Evaluating the Thermal Impacts of Different Masonry Wall Tie Designs Using FEM

by

Yue Shao

A thesis submitted in partial fulfillment of the requirements for the degree of

Master of Science

in

Civil (Cross-disciplinary)

Department of Civil and Environmental Engineering

University of Alberta

Abstract

A building's space heating system accounts for more than half of the total building's energy consumption. Reducing the energy use of space heating of buildings can decrease the national energy consumption of Canada and is helpful for sustainable development of the buildings. Improvement of thermal resistance of the wall is a reliable approach to decrease the energy consumption of the building. Masonry cavity walls are a commonly used type of exterior wall in Canada. They can provide reliable structural performance, considerable durability, and excellent thermal resistance. However, the presence of masonry ties, as a typical source of repeated thermal bridging, in the wall assembly significantly reduces the thermal resistance of the wall assembly.

Ties are considered a typical source of repeated thermal bridging in masonry cavity wall assemblies. Thermal bridging can cause thermal resistance reduction due to its high conductivity material penetrating the thermal insulation layers. Ties thermal bridging effect provide additional heat transfer pathways in the wall assembly. Codes and industry catalogues require the thermal impact of thermal bridging to be considered when calculating the thermal resistance of exterior walls. Although a few studies have been conducted on the effect of ties in reducing the thermal performance of walls, the thermal impact of ties has not been comprehensively studied. Incomplete thermal bridging reduction effect evaluation will result in insufficient HVAC system design and lead to energy consumption increases of buildings. Also, the ties thermal impact on the thermal resistance of the ventilated air gap has not been determined.

In this study, the effective thermal resistance of the ventilated air gap in masonry cavity walls considering ties thermal bridging impact was investigated, and the impact of ties on the thermal

resistance of wall assemblies was addressed with different influence factors. Based on the parametric analysis, effective methods to reduce ties thermal bridging effect were suggested. The effective thermal resistance of the ventilated air gap in masonry cavity walls was studied by using coupling computational fluid dynamics (CFD) and steady-state thermal analysis in Finite element method (FEM) modelling. In addition, a parametric analysis of the impacts of ties on the effective thermal resistance of a unit wall area was performed by using FEM with variations in ties material, insulation R-values, tie depth, tie spacing, grouting in concrete masonry blocks, and the effect of adding insulation around the tie. Based on the results, the tie's thermal bridging effects and ventilation in the air gap affect the thermal resistance of the air gap. And according to the parametric analysis, the tie material is the most influential factor of the ties' thermal bridging effect. The thermal resistance of the wall assemblies varies greatly with the change of tie material, ranging from 14.68%~41.85%. Using a low thermal conductivity material (e.g., GFRP tie) can almost eliminate the thermal bridging effect of the tie. Enlarging the tie spacing also can improve the overall thermal resistance of walls up to 12%. Using a low thermal conductivity tie material such as GFRP is recommended for effective thermal resistance improvement for the masonry cavity wall assembly.

Acknowledgements

I would like to take this opportunity to express my gratitude to my dear supervisor Dr. Yuxiang Chen, who guided me throughout this research and always gave technical advice, financial support, and kind encouragement. I would not have been able to finish this study without his help. I'd also like to thank him for bringing me into the field of building science.

I wish to extend my thanks to my groupmate Maysoun Ismaiel. She helped me with technical writing and provided many suggestions to improve my writing skills and readability of my papers.

My appreciation to Dr. Mark Hagel, engineering director of the Alberta Masonry Council, who always provided my research group with innovative and comprehensive information in the masonry industry. His information and ideas served as reasonable help and guidance to my research.

My sincere thanks to my MSc thesis defense committee members, Dr. Huazhou Li (Chair), Dr. Yuxiang Chen (Examiner and Supervisor), Dr. El Lobo Cruz Noguez (Examiner), and Dr. Samer Adeeb (Examiner), for their time and helpful suggestions.

Finally, I would like to thank my family for their endless love and support, which carried me through every difficulty in my life.

Table of Contents

List of Tables

List of Figures

Abbreviations

2D	Two-dimensional	-
3D	Three-dimensional	-
c	Specific heat	J/kg·K
CFD	Computational fluid dynamics	-
CMU	Concrete masonry unit	-
FEM	Finite element modelling	-
k	Thermal conductivity	W/m·K
h_c	Convective heat transfer coefficient	W/m^2
Nul	Nusselt number	-
q	Average heat flux value	W/m^2
R_a	Rayleigh number	-
R_{eff}	Effective thermal resistance of the model	$(m^2 \cdot K)/W$
$R_{eff.air\ gap}$	Effective thermal resistance of the air gap	$(m^2 \cdot K)/W$
R-value	Effective thermal resistance of the assembly	$(m^2 \cdot K)/W$
T	Temperature	K
T_m	Mean temperature	K
ΔT	Temperature difference	K
t	Thickness	mm
ρ	Density	kg/m^3
ε	Emissivity	-

1 Introduction

In many regions, a significant amount of energy is consumed due to building heating, cooling, and ventilation. In Canada, building energy consumption accounts for 28% of Canada's secondary energy. The space heating system is a major source of energy consumption in both residential and commercial buildings and it accounts for 61% and 55% of the total building's energy consumption, respectively (NRCan, 2014). Therefore, a reduction in the energy use of space heating of buildings is required to decrease the national energy consumption of Canada. In the other regions of the world, such as Europe, their building energy codes (EPBD recast) require designers to improve the thermal resistance values (R-value) of walls to be effective in the energy reduction approach (Capozzoli et al., 2013). Thermal resistance is the ability of a material or component to resist the heat flow. For the wall system, R-value is often to used to show the effective thermal resistance of the assemblies.

Masonry cavity walls can provide excellent thermal resistance, in addition to their sound durability and architectural appearance (Hendry, 2001). The superior physical properties of masonry, such as significant thermal mass, can reduce the energy usage in residential buildings and improve the thermal performance of exterior walls (Gregory et al., 2008). In addition, the air cavity can also be considered as the additional insulation layer. Therefore, the masonry cavity wall system can reduce energy consumption and create a comfortable living environment. However, one of the challenges that affects the thermal performance of masonry cavity walls is thermal bridging (ASHRAE, 2017a; Morrison Hershfield, 2018a). Thermal bridging in building envelopes occurs mostly in areas where structural components with high conductivity penetrate thermal insulation layers. In the case of masonry cavity walls, this phenomenon occurs through the ties, hangers, shelf angles, and insulation fasteners. The energy performance reduction caused by thermal bridging effect can reach 30% (Capozzoli et al., 2013; Tejedor et al., 2020).

Masonry wall veneer ties are used to hold brick veneers in place as well as connect the two wythes of the wall to act together to resist applied lateral loads and provide horizontal structural supports (CAN/CSA-A370-14, 2015). Ties are considered one of the typical sources of repeated thermal bridging in masonry wall assemblies. Tie material, geometry, and spacing can significantly impact the effective thermal resistance of masonry walls; the effective reduction can range from 3% to 25%, depending on the thickness of the insulation and other factors (e.g., type of the backup wall,

tie material) (Andrea Love, 2011; Wilson and Higgins, 2014). Therefore, research on the impact of masonry ties on the thermal performance of masonry exterior walls is necessary to enhance the efficiency of energy use in buildings and promote sustainable developments. There has been a production advancement in the shape, size, material, and alternate configurations of ties to improve thermal performance. Several tie types with different materials were introduced to the market to lower the thermal bridging effect. However, the quantification of their thermal performance has not been conducted. The research findings can guide manufacturing companies in optimizing and developing their products.

In addition to the thermal bridging impact of masonry ties, the effective thermal resistance of the air gap is also important to the overall thermal resistance of masonry cavity walls. Due to the low thermal conductivity of still air, an air gap in the wall assembly is considered an effective insulation layer. The weep holes on brick veneer provide access to connect the free air outdoor and the air inside the wall, causing the air gap to be ventilated. The vent openings provide additional heat loss paths from the indoor environment and complicate the thermal response of the wall assembly. Standards and codes provide the thermal resistance of a plane air gap in the wall assembly and several previous research activities have identified the air movement performance inside the air gap (ASHRAE, 2017b; ISO 6946, 2017; Sanjuan et al., 2011; Stovall and Karagiozis, 2004). However, further analytical investigations are required to determine the tie's thermal bridging effect on the thermal properties of an air gap. The presence of masonry ties and the vents coupling affect the thermal behaviour of the air gap. The complex multiple coupled phenomena may occur, such as three heat transfer mechanisms (conduction, convection, and radiation), resulting in a highly temperature-dependent air movement. Therefore, the thermal behaviour of the ventilated air gap is studied and presented first in this research.

1.1 Research Scope and Objectives

The objectives of this research are to identify the effective thermal resistance of the ventilated air gap and conduct parametric analysis to quantify the impact of masonry ties on the thermal performance of masonry cavity wall assemblies. Both objectives were conducted using a numerical analysis approach, FEM. The objectives of this research are summarized as follows:

- Evaluating the effective thermal resistance of the air gap ($R_{eff.air\ gap}$) in the wall assembly considering the thermal impact of the ties and ventilation by using a fluent model and steady-state thermal model, resulting in a reliable $R_{eff.air\ gap}$ value for the following research.
- Investigating and presenting the possible factors affecting the thermal impact of the tie on masonry cavity wall assemblies using FEM analysis. Potential factors such as the tie's material, shape, spacing, and CMU-backup wall's grouted condition are discussed in this study.
- Identifying the most effective optimization to reduce the additional heat loss caused by ties. Models with a thermal break around the tie body are studied.

Based on the results obtained from the models, some effective approaches are proposed to reduce the thermal bridging effect caused by ties to improve the efficiency of energy use in buildings. Suggestions of tie improvement can guide manufacturing companies in optimizing and developing their products. Therefore, research on the impact of masonry ties on the thermal performance of masonry exterior walls can significantly improve the efficiency of energy use in buildings and promote sustainable developments.

The masonry wall studied in this thesis is the CMU backup cavity wall, while the tie studied in this research is a slotted tie. The slotted tie is one of the most common types used in Canada. The slotted tie is more widely used in the construction area and has a more convenient installation due to its flexibility when accommodating differential height and movement between two wall layers (Hatzinikolas et al., 2015). Holes on the slotted tie plate minimizes thermal conductivity through the tie system causing the slotted tie (Figure 1.1) to have the highest thermal efficiency compared to the other tie types (Fero, 2015).

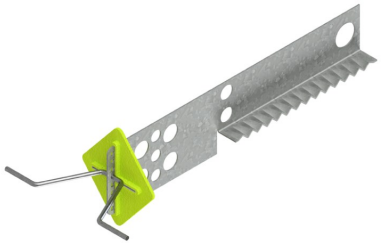

Figure 1.1: Schematic of slotted tie (source: Fero, Inc.).

Other than the tie shape, the tie material and tie spacing also play an essential role in generating thermal bridging and affecting the thermal resistance of the whole wall assembly. Galvanized steel and stainless steel are the most common materials used for ties. Galvanized steel is the most widely used tie material due to its affordable cost compared to stainless steel ties (Straka, 2013) and galvanized steel ties are the primary ties used in the models in this thesis. The maximum tie spacing is 800 mm in the horizontal direction by 600 mm in the vertical direction (Hatzinikolas et al., 2015). However, due to the proper block size and ease of installation, a spacing of 400 mm × 400 mm is frequently applied in construction.

1.2 Organization

This thesis is structured as follows:

- Chapter 1 introduces this thesis. The background on the masonry exterior wall, thermal bridging, masonry ties, and ventilated air gap is introduced. Research gaps are presented and discussed. The scope, motivation, objectives, and organization of the thesis are introduced.
- Chapter 2 provides background information on different tie types and commonly used tie materials in Canada, reviews of the thermal bridging effect on masonry wall assemblies, and the thermal properties of vertical air gaps in walls. Different approaches to determine the thermal resistance of the air gap and thermal transmittance of air voids in the wall assembly are introduced. Moreover, the methods and essential factors used to precisely simulate models are discussed in this chapter.

- Chapter 3 presents the methodologies used for the iterative modelling approach to determine the effective thermal resistance of the air gap as well as the steady-state thermal models of different tie materials, tie spacing, tie depth, grout condition, and tie insulation.
- Chapter 4 presents the results and discussion. The effective thermal resistance of the air gap and the effect of masonry ties on the thermal performance of exterior masonry walls are investigated and discussed in addition to a sensitivity analysis representing the influences of different parameters, such as tie materials, tie spacing, tie depth, grout condition, and tie insulation.
- Chapter 5 summarizes the conclusions derived from this study. Suggestions for more beneficial masonry ties are made and recommendations for future works are also presented.

2 Literature Review

Masonry ties are considered one of the most common thermal bridging sources in masonry cavity walls. Thermal bridging reduces the thermal resistance of walls and increases the energy consumption of buildings. This chapter provides a brief review of tie types and global designs. In addition, this chapter reviews the methods used to analyze the thermal properties of the air gap in wall assemblies. Different methods used to determine the convective heat transfer in air voids are also reviewed and compared.

2.1 Masonry Wall Tie Types

The thermal bridging effect is a challenge when evaluating the thermal resistance of masonry cavity wall assemblies. Inaccurate estimates of the thermal bridging effect can cause insufficient designs of the HVAC system in the building, a reduction in the comfort of occupants, and an increase in building energy consumption (ASHRAE, 2017a). There are two types of thermal bridging in the wall assembly: linear thermal bridging and point thermal bridging. Usually, linear thermal bridges are considered in the overall wall thermal transmittance calculations, while point thermal bridges are neglected. However, point thermal bridges can cause a significant reduction on the overall wall thermal transmittance.

In the cavity wall, masonry ties are evenly spaced and are considered a source of repeated point thermal bridging. The effective thermal resistance reduction of the wall assembly caused by a tie's thermal bridging effect can range from 3% to 25%, depending on the type of backup wall, nominal thermal resistance of the insulation, tie material, and tie shape (Wilson and Higgins, 2014). Previous research stated that the point thermal bridging components, such as brackets and ties, have a considerable impact on the overall thermal performance of the wall assembly and further research is required to quantify the influencing factors of the ties (Theodosiou et al., 2015). However, a tie's thermal bridging effect has not been considered in the codes and standards and little industry attention as well as detailed thermal analysis have been conducted to study the thermal resistance reduction caused by a tie's thermal bridging effect. Most of the literature studies and product analyses on masonry ties focus on its structural performance rather than thermal performance. Neither the NECB (2017) nor industry leaders have considered a tie's thermal bridging effect on the overall thermal transmittance (U-value) of a wall assembly.

Recently, Morrison Hershfield's (2018) introduced a building envelope thermal bridging guide that considers ties as part of the clear field. However, a more accurate evaluation of the wall's thermal resistance can help designers in devising more efficient HVAC systems and buildings by improving the thermal properties and energy efficiency of the wall assembly. The literature survey showed that a tie's shape, material, and distribution has a significant effect on thermal bridging (Theodosiou et al., 2015; Wilson and Higgins, 2014). This study provides additional insight into evaluating the impact of a tie's thermal bridging on the CMU-backup masonry cavity walls.

There are two general tie types in Canada: prescriptive ties and proprietary ties (CAN/CSA-A370-14, 2015; Drysdale and Hmid, 2005). Prescriptive ties have been summarized by Drysdale & Hmid (2005) and were described as nonadjustable ties with three shapes: corrugated strip ties, rectangular wire ties, and Z-wire ties (Figure 2.1). Prescriptive ties have limited application scope due to their fixed shapes that cannot adapt to the various heights of the wall as the two wall wythes in CMU backup masonry cavity walls typically have different mortar joint heights. Therefore, not all prescriptive ties can be used in CMU backup masonry walls, unless the veneer and backup wall use the same size masonry block. Proprietary ties are adjustable to accommodate variable mortar joint height differences between two wythes of the wall assembly and are more convenient to be used in practice (Figure 2.2). The slotted tie is the most commonly used type of tie in western Canada.

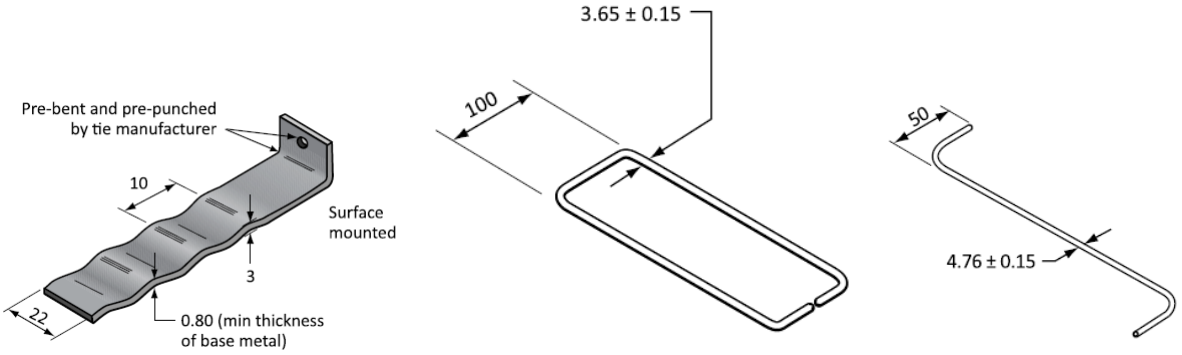

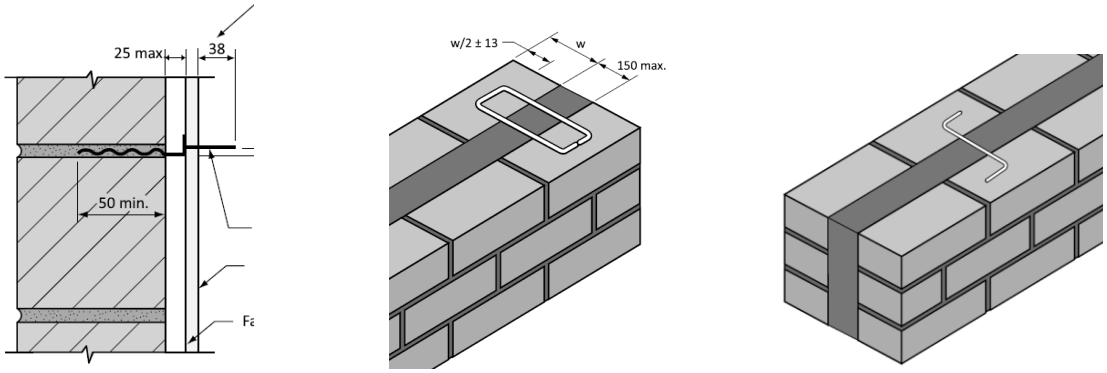

(a) Corrugated strip tie (b) Rectangular wire tie (c) Z-wire tie

Figure 2.1: Three examples of nonadjustable ties and tie placement in the wall (CAN/CSA-A370-14, 2015).

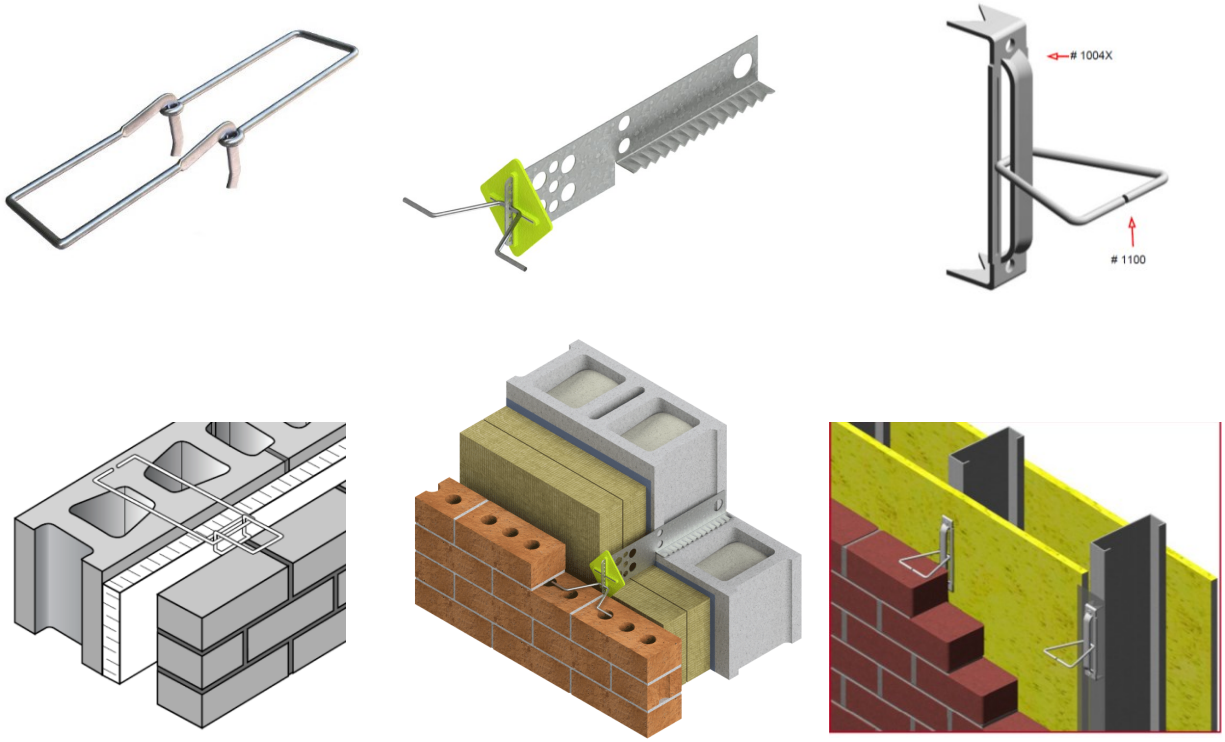

(a) Eye and Pintle Anchor (b)Slotted tie (c) Base and Vee Anchor

Figure 2.2: Three examples of adjustable ties (source: Hohmann & Barnard, Inc.; Fero, Inc., (CAN/CSA-A370-14, 2015)).

Other tie types are more commonly used outside of Canada. In the UK and Australia, wire ties and helical drive ties are commonly used in cavity masonry walls (Figure 2.3). Helical ties are drilled into the backup wall after the full construction of the two wythes, unlike traditional ties, which are placed in the wall during the wythe construction and can also be used as remedial ties (Leviat, 2021).

(a) Wire tie (b) Helical tie

Figure 2.3: Wire tie and helical tie (source: Leviat, Inc.).

Suggestions to reduce the thermal bridging effect caused by the ties have been studied in literature. Andrea Love (2011) found three methods to eliminate thermal bridging in the wall assembly: (1) by breaking the continuous thermal bridges by using different structural designs to move the high thermal conductivity components out of the insulation layer; (2) by using thermal breakers within the insulation boundary to impede thermal bridging, as thermal breakers form a thermal barrier in the insulation and decrease the extra heat flow through bridging; (3) by changing the thermal bridge component's material to a low thermal conductivity material when the component must pass through the insulation layer. Method 1 and 2 are inapplicable due to the tie's structural purposes. Therefore, changing the tie's material is the most suitable way to reduce the thermal bridging impact of ties.

Due to both structural and corrosion protection requirements, galvanized steel and stainless steel are the most commonly used materials for producing ties around the world (CAN/CSA-A370-14, 2015; Drysdale and Hmid, 2005). The use of galvanized steel ties or stainless steel ties are recommended depending on the environmental exposure conditions. Both materials are suggested

to be used in walls subjected to light environmental exposures. However, in the cases of moderate and severe environmental exposures, galvanized steel ties are specified to a sheltered exposure condition, while stainless steel ties can be used in any environmental exposure conditions without additional precautions (Straka, 2013). Stainless steel ties are almost twice as expensive as galvanized steel ones; however, the additional costs are relatively small compared to the overall cost of wall construction (Drysdale and Hmid, 2005; Straka, 2013). Although, stainless steel ties have a wider range of applications and many thermal and structural benefits, galvanized steel ties are still more commonly used.

Since steel ties have high thermal conductivity, ties made of composite material are produced for lower thermal conductivity, longer service life, and more stable structural performance. Straka (2013) and Lissel & Shrive (2001) tested the strength properties of ties made of fibre reinforced polymer composites (FRPC), such as glass fibre reinforced polymer ties (GFRP ties), and concluded that composite material ties could be applied in masonry cavity wall assemblies. Nevertheless, research regarding the thermal impact of these composite ties on wall assemblies is not available and must be addressed. Ties made of some innovative materials, such as materials with basalt fibres set in a resin matrix, were also studied, manufactured, and applied in construction (Ancon, 2021); however, the thermal impact of these innovative materials are not clear and requires further thermal testing and analysis. Compared to traditional steel ties, GFRP materials have considerably lower thermal conductivity (Inoue et al., 2013) and the thermal bridging effect caused by these ties is presumed to be significantly reduced.

2.2 Air Gap and CMU Air Voids in Double-Wythes Walls

A ventilated air gap plays an important role in the thermal performance of masonry wall assemblies. The air gap between the brick veneer and backup masonry wall is commonly ventilated through slots called “weep holes” at the upper and bottom areas of the brick veneer (Ibañez-Puy et al., 2017). Weep holes provide paths for moisture to drain from the wall assembly to avoid issues such as mould growth and rust among the building material, which can damage the building materials and reduce the building’s durability (Sanjuan et al., 2011; Theodosiou et al., 2015).

However, the vented airflow inside the cavity leads to a reduction in the thermal resistance of the exterior wall assembly in cold climate conditions. Several previous researchers focused on the

numerical analysis of opaque ventilated walls to determine the differential thermal properties between the ventilated wall and unventilated wall.

Sanjuan et al. (2011) made 3D CFD models to compare the thermal performance of unventilated and vented cavity wall assemblies. It was concluded that the open-joint ventilated cavity wall (a wall with weep holes) could cause more than 50% heat losses from indoor space during typical winter nights. Literature showed that under cold conditions, the openings on the veneer should be minimized to reduce additional heat loss through the wall assembly (Mingotti et al., 2011). Previous researchers ignored the thermal impact of the repeated thermal bridging ties on the thermal properties of the air gap when their models were set up.

To study the tie's thermal bridging effect on the ventilated air gap, the thermal properties of a ventilated air gap should be investigated first. ISO 6946 (2017) stated that the air gap in the wall assembly could be seen as a thermally homogeneous layer. Consequently, in the thermal resistance calculation of the wall assembly, the air gap can be seen as an equivalent building layer with the air's effective thermal resistance. Standards and codes, such as ISO 6946 (2017) and ASHRAE (2017), state the thermal resistance of the vertical air gap in the wall assembly. Different references have proposed various values as the values from different references are similar but not identical (ASHRAE, 2017b; CLEAR, 2004; Morrison Hershfield, 2018b; NSAI, 2017). The commonalities and differences of various references requirements are concluded below. The similar suggested requirements through all addressed references are: (1) the two bounded surfaces of the air gap should be parallel; (2) the air gap should be perpendicular to the heat flow direction; (3) the air gap's length and width should be 10 times that of the thickness (in the direction of heat flow) of the air gap. The thermal resistance of a vertical air gap in different references and their various applications are presented in Table 2.1.

Table 2.1: Suggested thermal resistance values of vertical air gaps

Type of vertical air gap	Thermal resistance ($m^2 \cdot K$)/W	Applicable Conditions
25-mm unventilated air gap[1] ISO 6946 (2017)	0.18	1. Emissivities[3] of the materials exposed to the air gap are not less than 0.8.
20-mm air gap ASHRAE (2017b)	0.22	1. Mean temperature of the air in the air gap is -17.8℃. 2. Temperature difference between two surfaces of the air gap is 5.6 K. 3. The effective emittance of the air gap is 0.82. 4. Values are applicable to ideal conditions (e.g., parallel surfaces are smooth and there is no air interchange with the indoor space).
25-mm air gap Morrison Hershfield (2018)	0.16	-
20-mm to 50-mm air gap CLEAR[2]	0.17	-

1. In ISO 6946 (2017), a 25 mm air gap with small ventilation openings (e.g., weep holes in the brick veneer) can be seen as an unventilated air gap.

2. CLEAR: Comfortable Low Energy Architecture, a multimedia teaching package that meets European and South Asia architecture requirement.

3. Most building materials' emissivity is greater than 0.8.

As shown in Table 2.1, based on ISO 6946 (2017), a 25-mm air gap with small ventilation openings (e.g., weep holes in the brick veneer) can be seen as an unventilated air gap. When the heat flow is in the horizontal direction and other conditions as shown in the table above, the thermal resistance of the air gap in the masonry cavity wall is 0.18 ($m^2 \cdot K$)/W. According to ASHRAE

Handbook Fundamentals, the thermal resistance of a 20-mm vertical air gap with horizontal heat flow is determined by considering the mean temperature of the air gap, the temperature difference between two surfaces of the air gap, and the emissivity of the material exposed to the air gap. When the mean temperature of the air in the air gap is -17.8℃ and the temperature difference between two surfaces of the air gap is 5.6 K, the thermal resistance of the air layer is 0.22 (m^2·K)/W (ASHRAE, 2017). The data used by Morrison Hershfield (2018) in their report is 0.16 (m^2·K)/W. A few online energy calculators also provide the thermal resistance of a vertical air gap. CLEAR (Comfortable Low Energy Architecture, a multimedia teaching package meets European and South Asia architecture requirement) mentioned that if the thickness of air layer was in the range of 20-50mm, the thermal resistance of the air gap should be 0.17 (m^2·K)/W.

In addition to the existing effective thermal resistance values of the air gap ($R_{eff.air\ gap}$, (m^2·K)/W), the thermal resistance of the air gap can be calculated using basic equations to meet the specific wall design. ISO6946:2007(E) provides an equation to determine the $R_{eff.air\ gap}$ value for unventilated air gap (Ujma and Umnyakova, 2019):

$$R_{eff.air\ gap} = \frac{1}{h_a + h_r} \tag{2.1}$$

Where h_a is the convective heat transfer coefficient (W/(m^2·K)) and depends on the temperature difference on the air gap surfaces (ΔT); h_r is the radiation heat transfer coefficient (W/(m^2·K)). Equations to obtain these two coefficients are shown below:

$$h_a = \begin{cases} 1.25, & \Delta T \leq 5\text{K} \\ 0.73 \times \Delta T^{\frac{1}{3}}, & \Delta T > 5\text{K} \end{cases} \tag{2.2}$$

$$h_r = E \cdot 4 \cdot \sigma \cdot {T_m}^3 \tag{2.3}$$

Where $E = \varepsilon_{1-2}$ is the emissivity factor of two parallel surfaces; σ is the Stefan-Boltzmann constant, 5.67×10^{-8} W/(m^2·K^4); T_m is the average temperature of the emitting surface and its surroundings (K). For the vertical air gap, T_m can be assumed to be the average temperature of the two surfaces of the air gap.

To address the detailed thermal performance in the air gap, including the thermal bridging effect caused by ties, the air gap can be solved by 3D computer models (ASHRAE, 2017). FEM is typically applied to solve a steady-state heat transfer in wall assemblies (Arendt et al., 2011;

Bontha et al., 2006; Fioretti and Principi, 2014). Unlike simplified equations mentioned in the code ISO6946:2007(E), these models require material properties for the convection, conduction, and radiation for the heat transfer analysis. Convective heat transfer is dependent on the height and depth of the air gap. The three heat transfer mechanisms are temperature-dependent with surfaces in the air gap. The complexity of computing heat transfer in the air gap is the main reason to analyse the wall by numerical analysis approach.

Computational fluid dynamics (CFD) in combination with FEM is a reliable method to model the dynamic air in the wall assembly and solve the thermodynamic problem of the wall. The results from the CFD analysis system can precisely present all detailed heat transfer performance in the model (Ibañez-Puy et al., 2017; Stovall and Karagiozis, 2004). Specific material, geometry, and boundary condition details are required in the model setup process to complete the simulation, such as the airflow direction, type, and velocity.

The air condition in the gap is one of the most critical setup conditions in the CFD model. The airflow direction in the air gap is always upward. As shown in Stovall and Karagiozis's research (2004), the main part of the cavity is laminar flow, while the air within the weep holes or complex geometric position is transitional flow or turbulent flow. Therefore, the air in the vertical air gap can be set as laminar flow. The air velocity in the air gap is related to the wind speeds in the outdoor environment. The natural convection effect in the air gap depends on the thermal buoyancy, wind speeds, and wind air direction. According to the experimental data quoted in Stovall and Karagiozis (2004), the air velocity in the air gap ranged from 0.05m/s to 0.15m/s when outdoor wind speeds were 1 m/s to 3 m/s, which was consistent with the results from CFD modelling.

In addition to the air gap in the wall assembly, the hollow CMU backup wall contains air in the CMU voids. ISO 6946 (2017) provided the calculation method for the divided unventilated air voids. The thermal resistance of the air voids, $R_{eff.air\ void}$ ($(m^2 \cdot K)/W$), can be calculated by:

$$R_{eff.air\ void} = \frac{1}{h_a + h_r} \tag{2.4}$$

$$h_r = \frac{4 \cdot \sigma \cdot {T_m}^3}{\frac{1}{\varepsilon_1} + \frac{1}{\varepsilon_2} - 2 + \frac{2}{\left(1 + \sqrt{1 + d^2/b^2} - d/b\right)}} \tag{2.5}$$

$$h_a = \begin{cases} \max(1.25, \frac{0.025}{d}), & \Delta T \leq 5\text{K} \\ \max(0.73 \times \Delta T^{\frac{1}{3}}, \frac{0.025}{d}), & \Delta T > 5\text{K} \end{cases} \quad (2.6)$$

$$\text{U} = \frac{1}{R_{eff.air\ void}} \quad (2.7)$$

Where ε_1, ε_2 are the hemispherical emissivity of the surfaces exposed to the air gap; d is the thickness of the air void (parallel to the heat flow direction) (m); b is the width of the air void (perpendicular to the heat flow direction) (m). For 8 inch CMU blocks, when the temperature difference between two faces of the block was 10 K and the mean temperature of the air was 300 K, the convective heat transfer coefficient h_a was 1.57 W/m^2·K while the h_r was 3.80 W/m^2·K, and the U-value was 5.37 W/(m^2·K).

The thermal transmittance evaluation of the air in the hollow CMU block in the backup wall can also be accurately solved using models. Previous studies have shown the importance of considering the influence of airflow within the cells of block units to simulate a reliable model (Martínez et al., 2018; Mooneghi et al., 2015). Henrique Dos Santos et al. (2017) conducted a numerical simulation of hollow concrete blocks to determine the average convective heat transfer coefficient in CMU voids. For 8 inch CMU blocks, the average convective heat transfer coefficient was 1.85 W/m^2·K, and the U-value of the block was 5.64 W/(m^2·K) when the temperature difference between the two faces of the block was 10°C. The difference between the models and the calculation results from the code was 5%.

2.3 Section Conclusion

This chapter provided a review of common tie types and methods to estimate the thermal resistance of air layers in the wall assembly. A tie's thermal bridging effect can have a considerable reduction in the thermal resistance on the masonry cavity wall. Based on the description above, the following key points are concluded:

(i) Adjustable ties, which belong to proprietary ties, are the ties used in masonry wall construction. The slotted tie is one of the most popular tie types in Canada. Galvanized steel and stainless steel are the most commonly used materials for ties and the thermal performance of the composite ties (e.g., GFRP) is required to be addressed further.

(ii) Previous studies have focused on the thermodynamic problem of the air gap in the wall assembly, but none of them have considered the tie's thermal impact on the air gap. The thermal resistance value of a 25-mm air gap in the wall assembly provided by different codes and reports ranges from 0.16 (m^2·K)/W to 0.22 (m^2·K)/W. Although these materials list the thermal resistance of the air gap, the values provided are not sufficiently accurate as the influence of the ties in the wall assembly was not considered.

(iii) The thermal resistance of the air gap can be determined in four ways:

a. selected from codes or standards;
b. empirical correlation method;
c. solved by steady-state thermal modelling;
d. solved by CFD models.

(iv) By comparing the results obtained from the codes with the results from previous research with similar conditions, it can be concluded that the U-values of the air voids in the CMU were similar (5.37 W/(m^2·K) and 5.64 W/(m^2·K), respectively) and the difference was 5%.

3 Methodology

Three-dimensional (3D) heat transfer analysis is a common method to evaluate the thermal performance of the masonry cavity wall. Traditionally, heat transfer in wall assemblies has been calculated under uni-dimensional (normal to the wall surfaces) heat transfer assumption, which neglects lateral heat transfer (Hassid, 1990). However, the thermal bridging effect in the wall introduces non-negligible lateral heat transfer. For instance, as one typical type of point thermal bridging in the wall assembly, the lateral heat transfer of ties in any direction cannot be ignored. Gao et al. (2008) showed that a uni-dimensional calculation of the thermal properties of a building envelope could result in a discrepancy of 10% to 40% compared to the total thermal transmittance from the testing data. Previous studies have also suggested that 3D analysis should be used to assess the thermal performance of masonry cavity walls to achieve higher accuracy (Gao et al., 2008; Theodosiou et al., 2015).

The finite element method (FEM) is used to learn the thermal impact of the ties on the thermal performances of masonry exterior walls. Due to the 3D heat transfer analysis required for the masonry cavity wall, multi-dimensional computer models and experiments are popular research methods to evaluate the thermal performance of the wall with thermal bridging (ASHRAE, 2017b). FEM is a reliable simulation method; it is capable and flexible when simulating and solving complicated cases with acceptable accuracy, while experiments are more expensive and time-consuming. Therefore, only FEM was conducted in this research and the 3D FEM software ANSYS Workbench 2019 R3 was selected to build and analyze all models in this study.

In the first part of this thesis, an iterative modelling process coupling CFD and steady-state thermal analysis was used to investigate the effective thermal resistance of the ventilated air gap. In the second part, with the air gap's thermal resistance determined, a steady-state thermal analysis was used to perform parametric analysis on the design of masonry ties.

When determining the effective thermal resistance of the air gap, the models considered two variables: (1) different nominal thermal resistance of the insulation board from R5 to R25; and (2) different air velocities in the air gap (0.05m/s, 0.1m/s, and 0.15m/s).

After the effective thermal resistance of the air gap was obtained, five groups of parameters were discussed for analysis:

- Different grout conditions in the CMU backup wall;
- Different tie material and insulation R-value;
- Different tie depth in the backup wall;
- Different tie spacing;
- Adding an insulation cover for different thicknesses around the tie body.

3.1 Thermal Analysis for the R-value of the Air Gap

The thermal bridging impact of ties on the exterior masonry walls is interrelated with the vented air gap. When the air gap is an enclosed space, all heat loss exits through the brick veneer, as shown in Figure 3.1(a). Alternatively, when the air gap is ventilated, the vented air flow in the air gap carries additional heat loss through the weep holes in the brick veneer, as shown in Figure 3.1(b). The presence of a tie's thermal bridging effect leads to extra heat loss from the indoor space and the cold air from outside lowers the temperature of the air gap, causing an increase in the tie's thermal bridging effect. The ventilated air gap increases a tie's thermal bridging impact on the wall assembly and decreases the overall thermal performance of the wall, while the repeated point thermal bridging influences the thermal resistance of the air gap. The effective thermal resistance of the air gap ($R_{eff.air\ gap}$ (m^2·K/W)) can be calculated using Eq.(3.1):

$$R_{eff} = \frac{\Delta T}{q} \tag{3.1}$$

Where ΔT is the temperature difference (K) between the hot and cold surfaces of the model and q is the measured average heat flux (W/m^2) through the surfaces of the air gap's hot side. The temperature difference between the two surfaces of the air gap varies when the ties place in the air gap and the heat flux value through the wall increases due to the impact of the tie's thermal bridges, leading to extra heat loss. As a result, the effective thermal resistance of the ventilated air gap changes when repeated ties through it.

The complex multiple coupled phenomena occurs, such as three heat transfer mechanisms and a highly temperature-dependent air movement, and the thermal properties of the ventilated air gap should be studied first in this research.

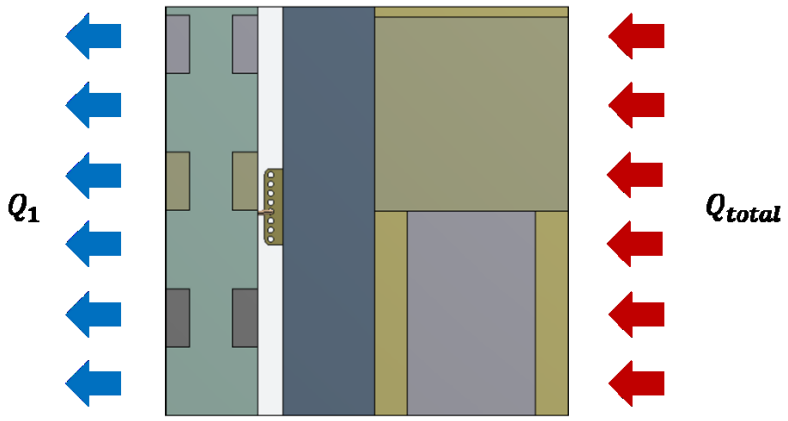

(a) Heat flow path of an unventilated wall

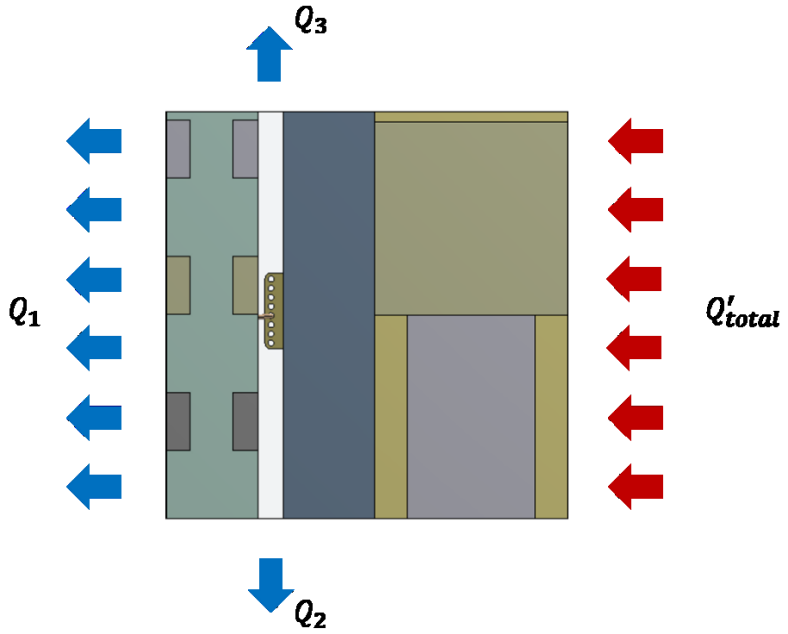

(b) Heat flow path of a ventilated wall

Figure 3.1: Heat transfer path through the wall assembly.

Due to the difficulty in identifying the complex relationship between the ventilated air and the ties by known empirical correlation, CFD simulations are used in this research. Thermo-fluid dynamic behaviour should be considered to investigate the concrete masonry cavity walls to simulate the wall's condition under the real air flow (Henrique Dos Santos et al., 2017; Laaroussi et al., 2017; Sun and Fang, 2009). CFD simulations have been used to simulate the vented air flow in the air

gap as the first step in calculating the overall R-value for different wall configurations. The unstructured mesh discretization method of the CFD modelling in Fluent system is Finite Volume method (FVM).

An iterative modelling process that couples CFD and steady-state thermal analysis was set up. ANSYS Fluent was employed to solve conservation equations for conjugate problems in the air gap. Fluent is a 3D fluid analysis system for CFD modelling in ANSYS Workbench; however, the fluent tutorial did not recommend that the CFD models contain many solid components. Meanwhile, steady-state thermal modelling in ANSYS Workbench is more accurate and easier to estimate the heat transfer between solid components. Therefore, a modelling process coupling the Fluent and steady-state thermal analysis system was used. Initially, a simplified model was solved in Fluent by CFD to obtain the air performance in the air gap and a detailed model was processed in a steady-state thermal modelling based on the preceding result. As the models' results cannot converge in one iteration, iterative modelling is required.

3.1.1 Typical Configuration of Masonry Wall Assembly

To determine the thermal impact of air flow inside the wall assembly, physical details of a masonry wall assembly must be learned. The typical configuration of the wall assembly is presented in Figure 3.2. The air gap's design width is usually 25 mm. The ties used to connect two wythes of the masonry cavity wall should be adjustable ties. The level of insulation panel set in the wall varies according to the climate area of the building site. Due to Canada's cold climate condition and the common practice in construction, galvanized steel ties and R15 or more insulation board are always used in wall assemblies.

The difference between R-value and R15 is the former is the effective thermal resistance of the assemblies, and the latter is the nominal thermal resistance of the component with the imperial unit. The effective thermal resistance is the total resistance of the assemblies, which includes the surface film resistance, contact resistance and other thermal impacts between components, while the nominal thermal resistance is determined by the component material's conductivity. R-value can be used for both imperial unit and SI unit. 'R15' represents that the nominal thermal resistance of the insulation board is 15 $\frac{ft^{2}\cdot{}^{\circ}\mathrm{F}\cdot hr}{Btu}$. The 'R' is used as an imperial unit for the thermal resistance, while the figure is the nominal R-value of the insulation.

For the purpose of easy comparison and analysis of different models in the subsequent studies, the wall model was labelled with an ID of 'WGXX' ('W' stands for whole masonry wall assembly, 'G' represents galvanized ties that are used in the wall, and 'XX' is the insulation level used in the wall assembly). For example, the wall assembly with R15 exterior insulation was labelled as 'WG15'. All material properties of the wall components are listed in Table 3.1.

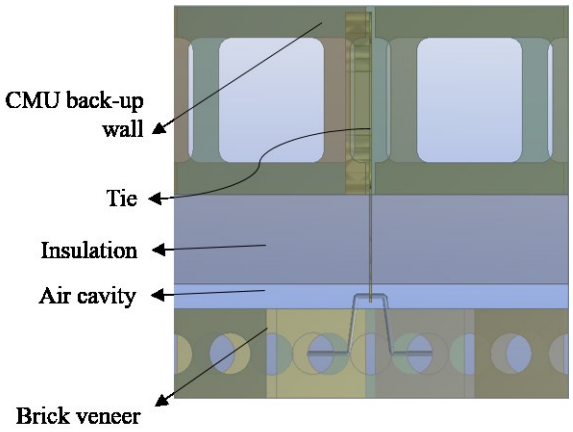

Figure 3.2: Horizontal cross section of the wall assembly.

Table 3.1: Material properties of the wall components

Components	Thermal Conductivity k (W/m·K)	Density ρ (kg/m^3)	Specific Heat Capacity c (J/kg·K)	Thickness t (mm)	Emissivity ε
Brick	0.78			90	0.93
Cement mortar	0.5			-	
Empty CMU block	0.87	1800		190	0.855
Mineral wool board	0.034	70	840	90 (R15)	
Masonry tie (Galvanized)	62	7800	470	1.61 (16 gauge)	0.6
Air in CMU voids	0.026	1.1614	1007		
Exterior air film	0.0333			1	
Interior air film	0.00833			1	

3.1.2 Fluent Model Description

To perform the CFD modelling in the Fluent model, an equivalent model was generated by simplifying the actual details. The geometry constituted three bulk layers: 90-mm equivalent brick veneer, 25-mm air gap fluid layer, and an equivalent insulation-CMU-backup wall layer. The horizontal cross-section of the WG15 model is shown in Figure 3.3. The dimensions of the model are 2.8-m in height by 0.4-m in width, which was determined by the typical wall height and horizontal tie spacing. Seven ties were evenly spaced along the vertical middle line of the model and the cross-sectional dimensions of the ties were 1.59 mm × 75 mm. The simplified geometry is presented in Figure 3.4.

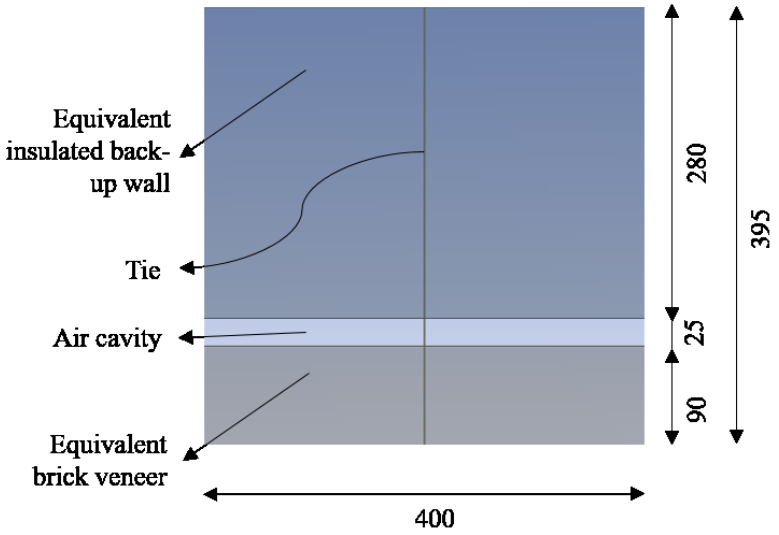

Figure 3.3: Horizontal cross section of the fluent model (mm).

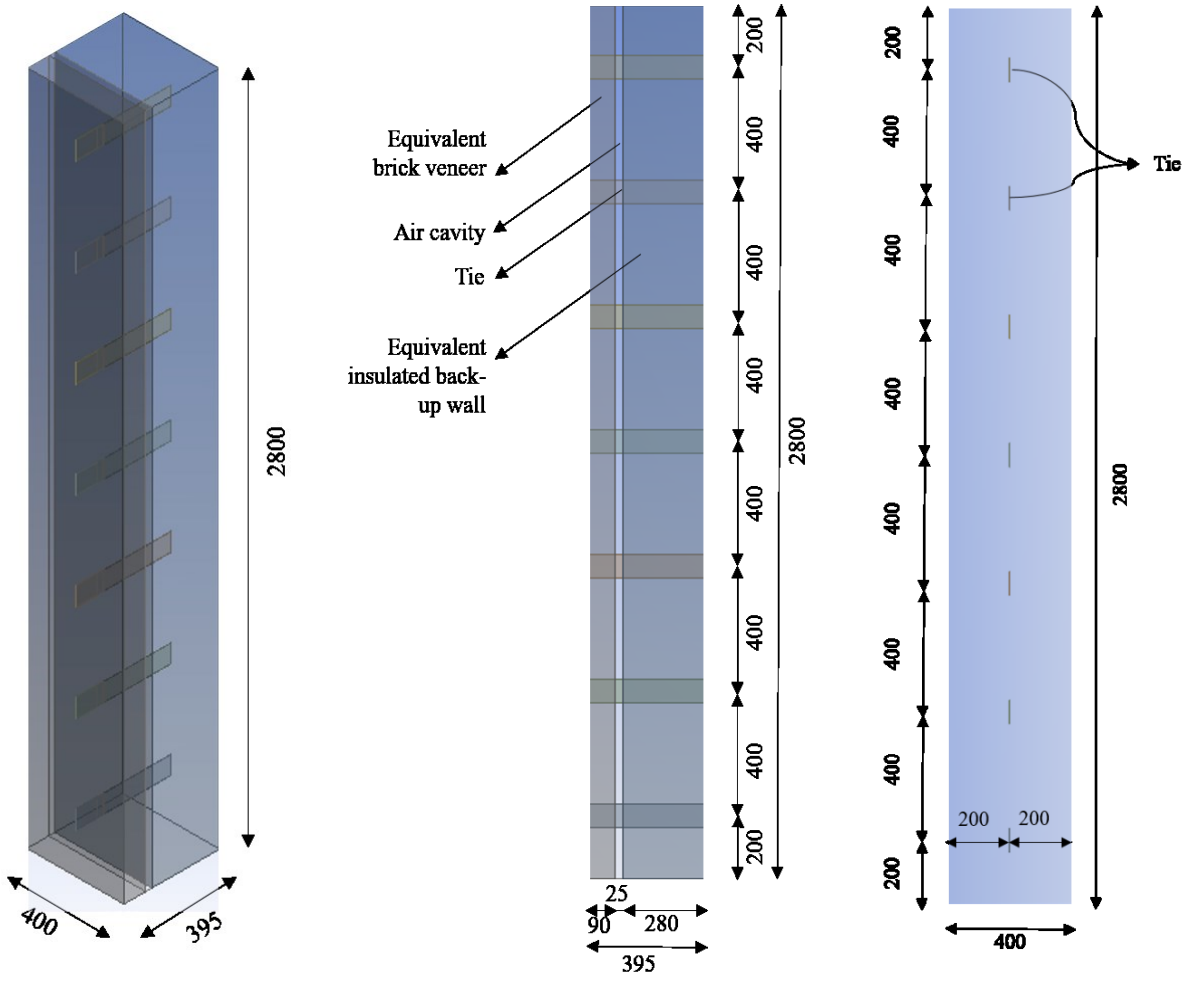

(a) isometric view (b) cross-section (c) front view

Figure 3.4: Geometry of WG15 in fluent modelling (mm).

Conductive, convective, and radiative heat transfer are considered within each wall system. The numerical models were developed using mixed convective and radiative boundary conditions to simulate the external environment and the air cavity boundary conditions. Four properties were set for the boundary conditions: (1) temperatures for the indoor and outdoor environment, (2) emissivity, (3) heat transfer coefficients, and (4) air velocity in the air gap. The indoor and outdoor temperatures applied in this model were $T_{outdoor}$ = -18°C and T_{indoor} = 21°C in contact with the specimen surfaces as shown in Figure 3.5 (ASTM C1058, 2015; NECB, 2017). The radiation in the fluid domain was surface to surface radiation.

The air film on the exterior or interior surface is treated as a 10-mm solid layer with thermal resistance equivalent to the combined convective and radiative heat transfer coefficients, 0.03 and 0.12 m^2·K/W for exterior and interior air films, respectively (Ashrae, 2017; Morrison Hershfield, 2018b). The corresponding thermal conductivity of the solid layer can be obtained below:

$$k = \frac{1\ mm}{R} \tag{3.2}$$

where t is the thickness of the air film (1 mm), resulting in a $k_{exterior.air}$ and $k_{interior.air}$ of 0.0333 W/m·K and 0.00833 W/m·K, respectively.

The air flow inside the air cavity is always from the bottom to the top. Stovall & Karagiozis (2004) found the air in the air gap could be assumed as laminar air. The air flow rate range inside the air gap is from 0.05 m/s to 0.15m/s from the results of Kuenzel and Mayer's experimental data for environmental wind speeds from 1 m/s to 3m/s. Therese K's CFD model also validated the range (Stovall and Karagiozis, 2004). Thus, the air speeds in the fluent models were assumed as 0.05 m/s, 0.1 m/s, and 0.15 m/s. Two sidewall surfaces (indicated by the two red dashed lines in Figure 3.5) were set as a periodic boundary condition and a whole wall's thermal properties could be obtained by only solving this 400-mm width model. The top and bottom end walls' surfaces were assumed as adiabatic surfaces. For illustration, specimen WG15's boundary conditions in the fluent model are shown in Figure 3.5.

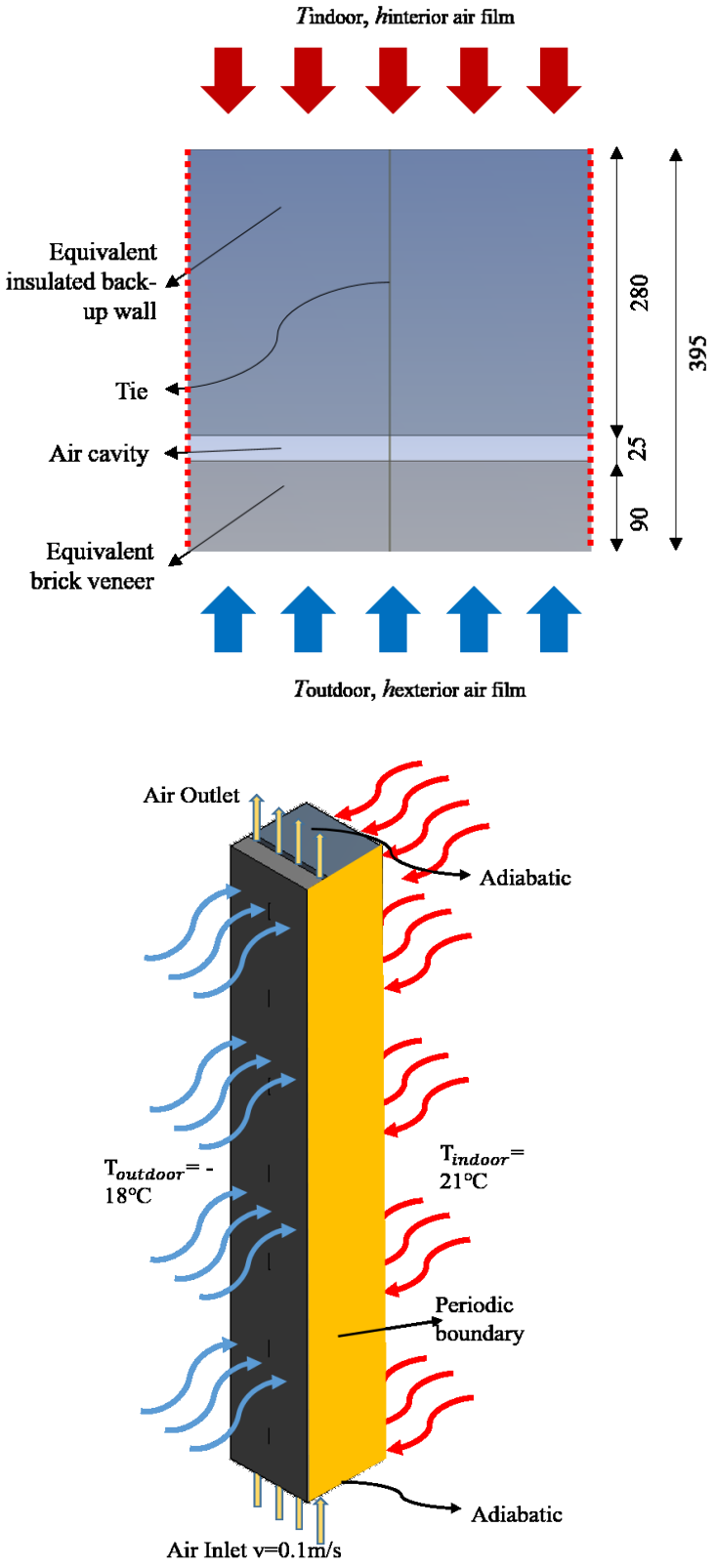

Figure 3.5: Boundary conditions of the specimen in fluent modelling (mm).

Based on the theory of FEM, the mesh size selection provides a considerable impact on the final results of each model. The fluent model WG15 was set up to determine the most efficient mesh size of the models. The simulated R_{eff} value ($m^2 \cdot K/W$) of the model was calculated using Eq. (3.1), where q is the measured average heat flux (W/m^2) through the specimen's hot side surfaces. The R-values of the WG15 model in fluent modelling solved under the range of mesh size 0.01 mm to 0.007 mm were identical at 1.980 $m^2 \cdot K/W$.

Fluent uses the FVM to solve the CFD models. One of the difference between the FVM and FEM is FVM uses the cell-centred finite volume approach while the FEM uses nodes on meshed element's corners and border lines. FVM can be a special case of FEM when certain conditions are satisfied (Molina-Aiz et al., 2010). For the incompressible ideal gas, the energy equation solved by Fluent is shown below (ANSYS, 2021):

$$\frac{\partial}{\partial t}\left(\rho\left(e+\frac{v^2}{2}\right)\right)+\nabla\cdot\left(\rho v\left(h+\frac{v^2}{2}\right)\right) = \nabla\cdot\left(k_{eff}\nabla T-\sum_j h_j\,\overrightarrow{J_J}+\ddot{\tau}_{eff}\cdot\vec{v}\right)+S_h \tag{3.3}$$

$$e = \mathrm{h}-\frac{p_{op}+p}{\rho} \tag{3.4}$$

$$h = C_pT+\frac{p}{\rho} \tag{3.5}$$

$$h_j = \int_{T_{ref}}^{T} C_{p,j}\,dT \tag{3.6}$$

Where ρ is the density of the fluid (kg/m^3); v is the velocity of the fluid (m/s); k_{eff} is the effective conductivity of the fluid ($W/(m\cdot K)$); $\overrightarrow{J_J}$ is the diffusion flux of species j; S_h is the source of energy; C_p is the specific heat capacity of the fluid; p is the gauge pressure; p_{op} is operating pressure; $\nabla\cdot$ represent the divergence operator, which means $\begin{Bmatrix}\frac{\partial}{\partial x}\\ \frac{\partial}{\partial y}\\ \frac{\partial}{\partial z}\end{Bmatrix}^T$, $\nabla\cdot(k_{eff}\nabla T)$ represents heat transfer caused by conduction, $\nabla\cdot(\sum_j h_j\,\overrightarrow{J_j})$ represents heat transfer caused by species diffusion, $\nabla\cdot(\ddot{\tau}_{eff}\cdot\vec{v})$ represents the heat transfer caused by viscous dissipation.

The energy equation solved by FEM is presented below, this equation is based on the first law of thermodynamics that thermal energy is conserved in a system (ANSYS, 2021).

$$[C_e^t]\{\dot{T}_e\} + ([K_e^{tm}] + [K_e^{tb}] + [K_e^{tc}])\{T_e\} = \{Q_e^f\} + \{Q_e^c\} + \{Q_e^g\} \quad (3.7)$$

Where $[C_e^t]$ is the element specific heat matrix; $[K_e^{tm}]$ is the element mass transport conductivity matrix; $[K_e^{tb}]$ is the element diffusion conductivity matrix; $[K_e^{tc}]$ is the element convection surface conductivity matrix; $\{Q_e^f\}$ is the element mass flux vector; $\{Q_e^c\}$ is the element convection surface heat flow vector; $\{Q_e^g\}$ is the element heat generation load.

The difference between CFD and FEM, is that CFD focuses on the heat transfer due to the fluid properties, while the FEM uses a general energy equation to solve models; for example, the energy equation solved by CFD includes the term of heat transfer due to viscous dissipation. Therefore, in this study, CFD is used to solve the heat transfer in the fluid area, and FEM is used to solve the heat transfer in solid components.

3.1.3 Steady-State Thermal Modelling Description

Simulating insulation and CMU block in steady-state thermal modelling with its actual dimensions is more accurate than the simplified model in Fluent. Unlike the brick veneer, which has a relatively uniform thermal conductivity, the geometry and material properties of the insulation and CMU backup wall vary significantly due to the presence of ties. FEM models cannot estimate the actual heat transfer pattern by using the equivalent insulation and CMU backup wall as the components in the assembly. Therefore, it is necessary to build a model for insulation and backup wall layer with detailed configuration in steady-state thermal modelling to estimate the accurate heat transfer. The geometry of the components in the model was determined by its physical dimensions. The geometry of this model is shown in Figure 3.6.

In the steady-state thermal modelling, the boundary conditions were indoor design temperature and the temperature distribution imported from the fluent model. And all other surfaces were adiabatic. Specimen WG15's boundary conditions in the steady-state thermal analysis are shown in Figure 3.7.

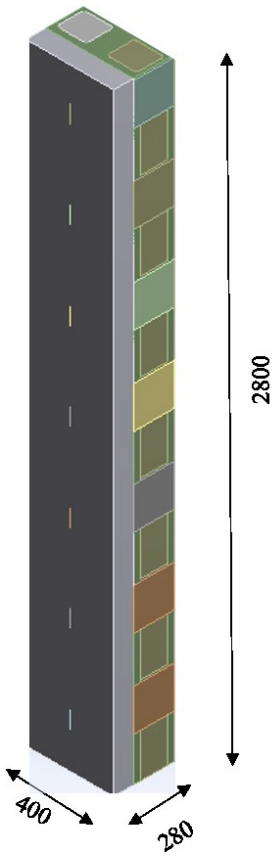

Figure 3.6: Geometry of the model in steady-state thermal modelling in iterative model (mm).

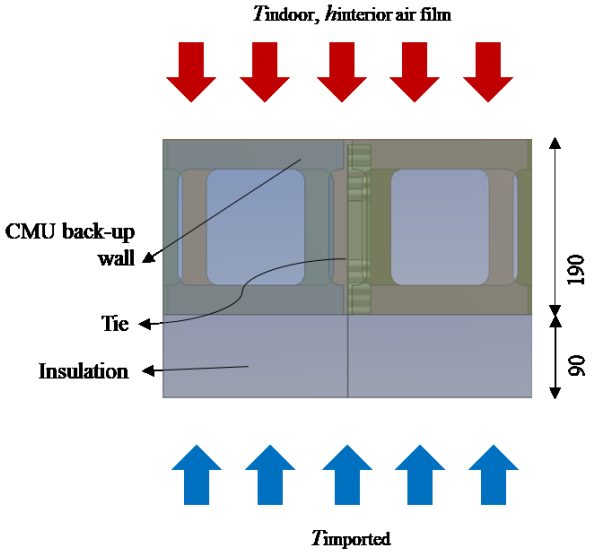

Figure 3.7: Boundary conditions of the WG15 in steady-state thermal modelling (mm).

A 400 mm × 400 mm masonry wall model with R15 exterior insulation was built in the steady-state thermal modelling to determine the most efficient mesh size of the models. The model's geometry is shown in Figure 3.8. For the sake of discussion, this model was named 'Unit model'. This Unit model was assumed only to have conductive heat transport. The model was solved by steady-state thermal analysis and the heat flux value through the Unit model could be obtained from the models' solution. The simulated R_{eff} value ($m^2 \cdot K/W$) of the model was calculated using Eq.(3.1). The R_{eff} values of the model under different mesh sizes are shown in Figure 3.9 and the trend line converges at mesh size of 0.007 mm, which was the mesh size selected in the steady-state thermal models. Figure 3.10 shows meshed Unit model with mesh size of 0.007mm.

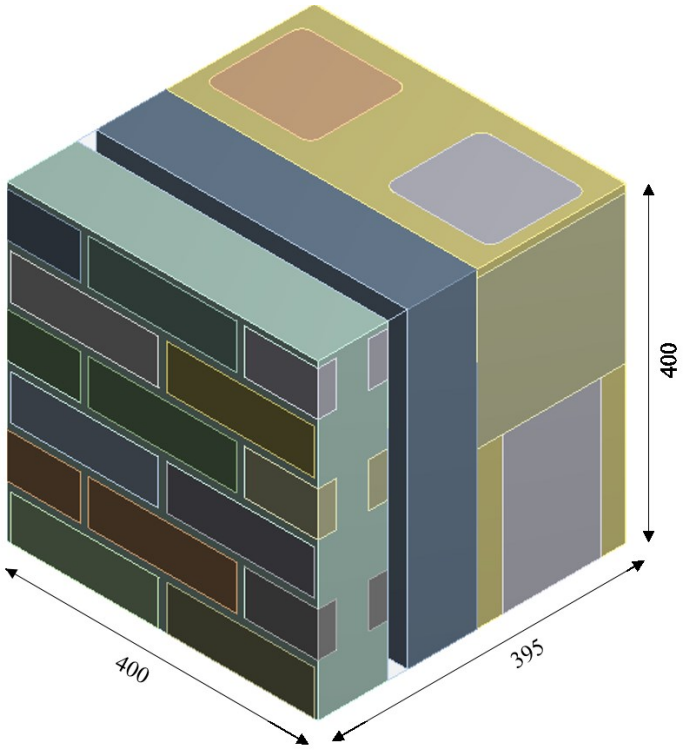

Figure 3.8: Unit R15 model for mesh size determination (mm).

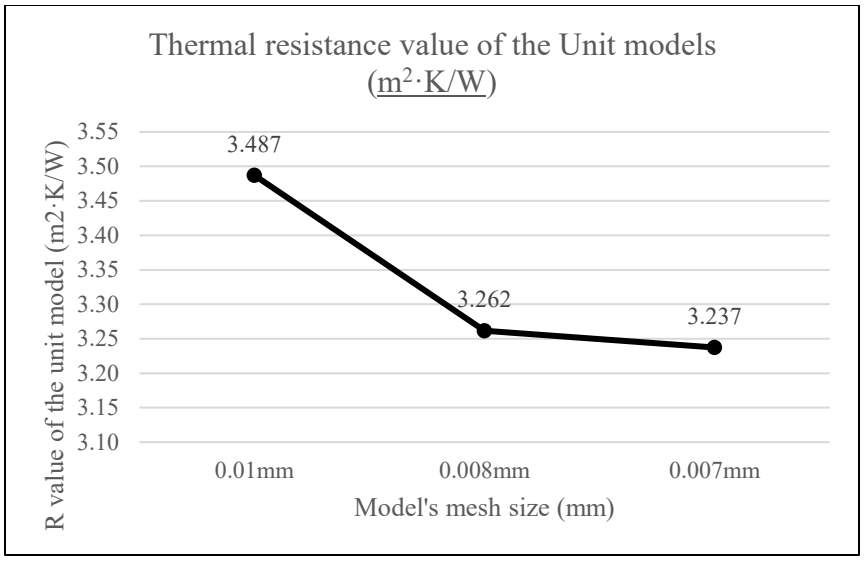

Figure 3.9: R-value of the Unit model under different mesh size (m^2·K/W).

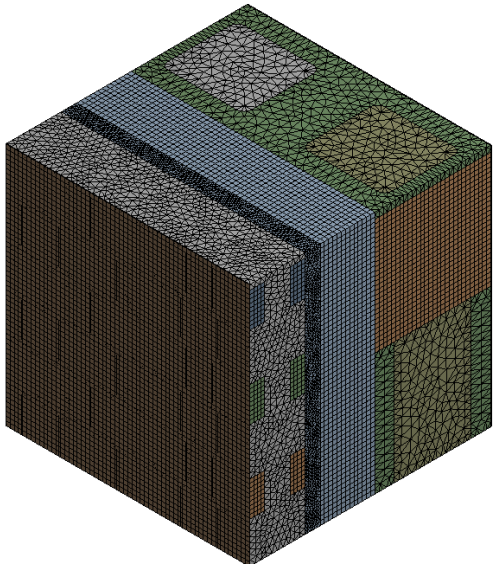

Figure 3.10: Meshed Unit R15 model.

The R-values of the WG15 model in fluent modelling solved under a mesh size of 0.007 mm to 0.01 mm were consistent at 1.980 m^2·K/W. Therefore, to facilitate the data transfer between two different analysis systems, the mesh size in the fluent modelling was also selected to be 0.007 mm. The meshed air gap is shown in Figure 3.11. Only part of the meshing is displayed in order to show the meshes clearly.

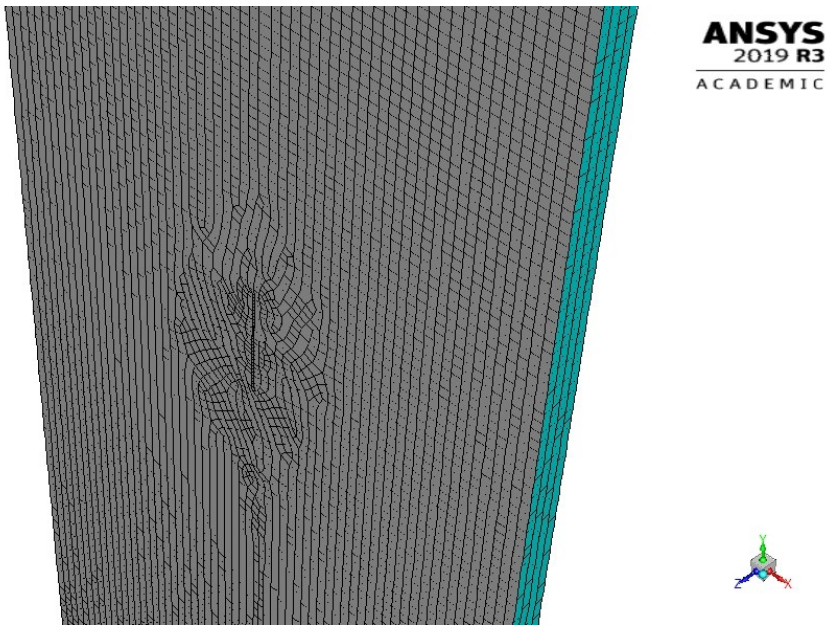

Figure 3.11: Meshed air gap component in WG15 model.

Two models, with one only containing brick veneer and the other with the insulation and CMU backup wall, were built in steady-state thermal modelling to determine the equivalent R-values of two bulk wall layers used in the Fluent models; $R_{equv.brick}$ (m^2·K/W) for the R-value of the equivalent brick veneer and the $R_{equv.insulation_{CMU}}$ (m^2·K/W) for the R-value of the equivalent insulation and CMU layer (Figure 3.12). A specific temperature difference was set up on the two sides of the models. Two equivalent R-values were calculated using Eq. (3.1). The equivalent *R-value*s (R_{equv}) were then converted to the thermal conductivity to import the properties of the wall into the Fluent models, as shown below:

$$k = \frac{t}{R_{equv}} \tag{3.8}$$

where t is the thickness of the model.

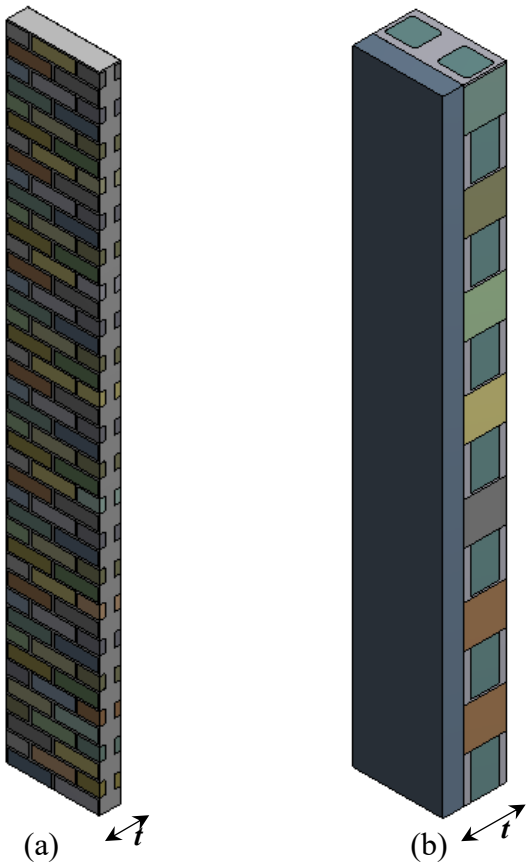

Figure 3.12: Models for equivalent R-values determination: (a) the model to obtain $R_{equv.brick}$; (b) the model to obtain $R_{equv.insulation_{CMU}}$.

3.1.4 Iterative Modelling Process

Figure 3.13 shows the flowchart of the iterative model. The initialization started from the Fluent modelling and the indoor and outdoor temperatures were set as two boundary conditions at the interior and exterior surfaces of the wall assembly. The air inlet and air outlet were set at the bottom surface and top surface of the air gap, respectively. The Fluent model solution provided the approximate temperature distribution on the interface of the insulation and the air gap, which included the thermal impact of the vented air passing through the metal ties. The obtained temperature distribution was then input into the steady-state thermal model, along with the interior surface temperature, to determine the average heat flux value on the interior surface.

The average heat flux value on the interior surface was selected as the connection setup between the two types of modelling. The average value was determined by the average of the heat flux values at all mesh nodes on the interior surface. As shown in Figure 3.1, the average heat flux value on the interior surface can reflect the total heat transfer through the specimen. As the temperature cannot be updated after simulation, the average heat flux value on the interior surface was taken instead of using the temperature distribution to accomplish the following iterative modelling. Once the temperature was imported to the interior surface in the following model, the values are fixed and cannot be updated after the simulation of the model is completed and the subsequent iteration process cannot be carried out. In addition, the heat flux values of the ties on the interface between the air gap and insulation are too high, which can cause a huge margin of error in the heat transfer of the wall assembly. As a result, the average heat flux value on the interface between the air gap and insulation cannot be used. The average heat flux value on the interior surface of the wall, together with the exterior surface temperature, can simulate the heat transfer in the wall assembly. Therefore, the obtained average heat flux value on the interior surface was chosen as the connection between the two types of the analysis system.

The average heat flux value through the specimen can be obtained by one coupling Fluent-steady-state-thermal iteration. The resulting heat flux through the steady-state model assembly was input as the new hot side boundary condition on the surface of the backup wall in the next iteration's fluent model. The iterative model continued running until the calculated R_{eff} value of the wall assembly converged.

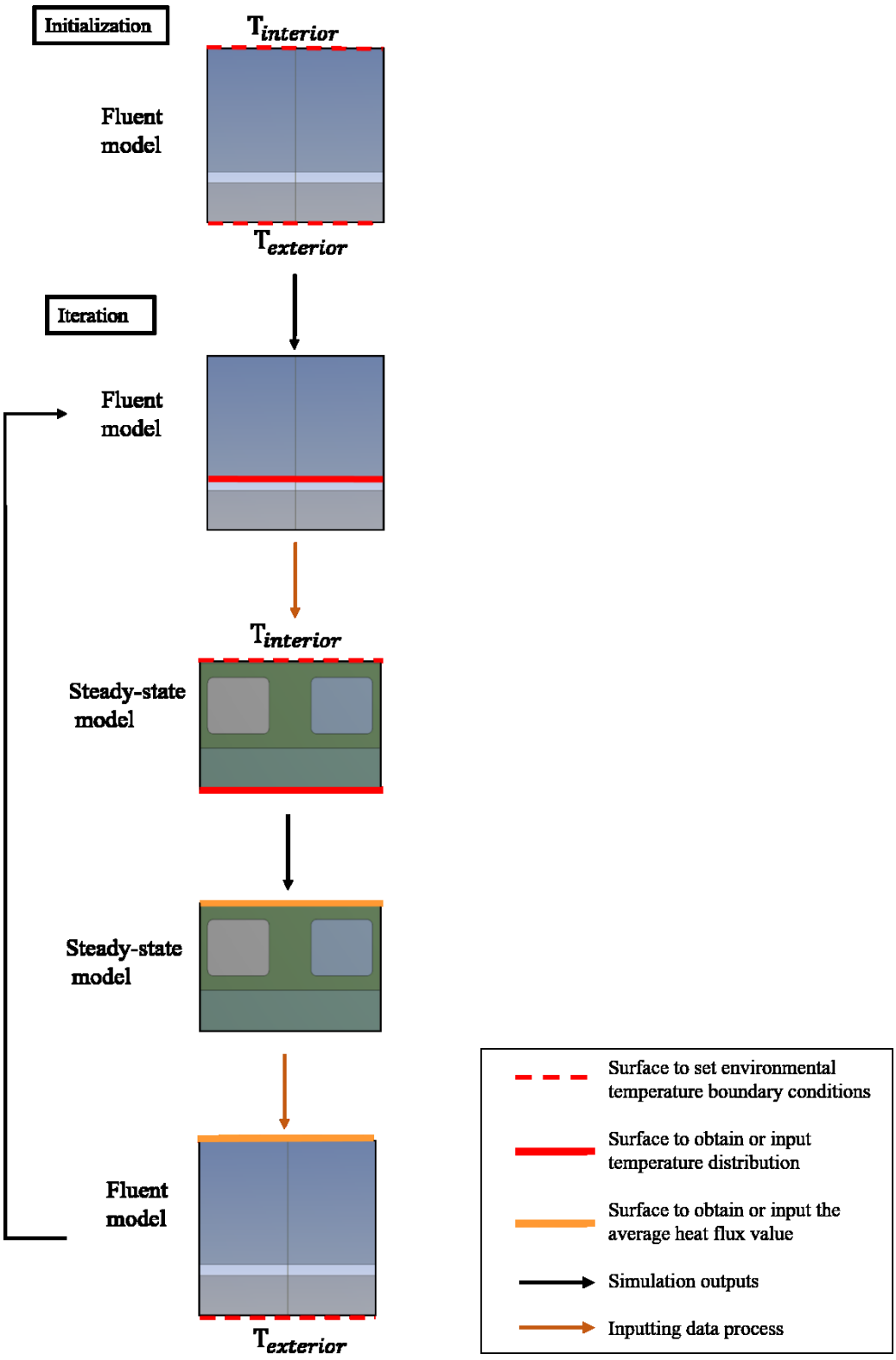

Figure 3.13: Flow chart of the iterative model.

Specimen with different configurations were learned to determine the range and the regularity of the air gap's effective thermal resistance. Model WG15 was simulated to be the reference of comparison. The results are divided into two main groups: (1) the comparison between cases with different insulation R-values; and (2) the effect of air velocity on the thermal performance of the air gap. All cases mentioned above are ungrouted. The concrete cores can be seen as filling the still air inside. The IDs of studied models are listed in Table 3.2.

Table 3.2: Specimen ID for models with different configurations

Specimen Size		2.8 m × 0.4 m			
Tie Configuration		No-tie	Galvanized tie	Galvanized tie	Galvanized tie
Air Velocity in Air Gap		0.1 m/s	0.1 m/s	0.05 m/s	0.15 m/s
R-value of Rigid Insulation	R5	WN5	WG5	WG15_V0.05	WG15_V0.15
	R10	WN10	WG10		
	R15	WN15	WG15		
	R20	WN20	WG20		
	R25	WN25	WG25		

Note:

First character: 'W' represents the whole wall cases, 2.8 m x 0.4 m.

Second character: tie with different material ('G' represents galvanized steel tie; 'N' represents the wall that no-ties set in the wall assembly).

Figures: R-value of the rigid insulation board in the wall assembly.

Characters after the "_": 'V' represents air velocity. The values are the air speeds in the air gap.

The thermal resistance in the system is shown in Figure 3.14 and the effective thermal resistance value of the air gap ($R_{eff.air\ gap}$) highlighted in the system schematic is the ultimate aim of the modelling in this section. Eq. (3.9) was used to obtain the effective thermal resistance of the system.

$$\frac{1}{R_{equv.brick} + R_{air\ gap}} + \frac{1}{R_{air\ loss1}} + \frac{1}{R_{air\ loss2}} + R_{equv.insulationCMU} = R_{eff} \qquad (3.9)$$

The calculated $R_{eff.air\ gap}$ is the effective thermal resistance of the air gap. The heat flux value through the assembly used the average heat flux value on the interior surface, which can be

obtained from the steady-state thermal models' output. The simulated R_{eff} was calculated using Eq. (3.1).

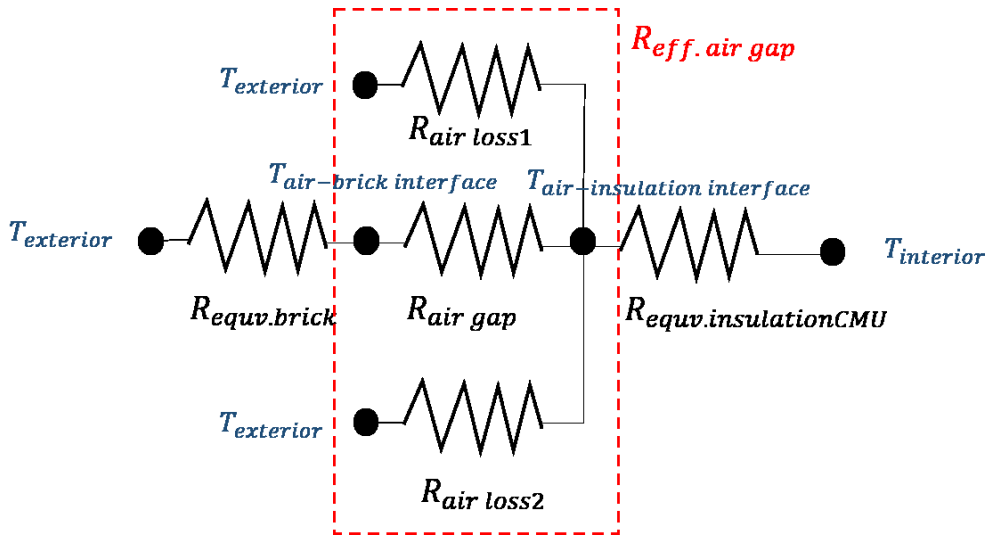

Figure 3.14: Schematic of the thermal resistance of the system.

Two methods were determined to calculate the $R_{eff.air\ gap}$ value within the wall. For the first calculation method (Method I), due to the designated set up in the steady-state thermal models, the air gap was seen as the component completely in series with other components in the model (Figure 3.15). The $R_{eff.air\ gap}$ can be determined by comparing the resulted R_{eff} value with the sum of R-values of two equivalent solid layers. The $R_{eff.air\ gap}$ (m^2·K/W) can be calculated by Eq. (3.10):

$$R_{eff.air\ gap} = R_{eff} - R_{equv.brick} - R_{equv.insulation_{CMU}} \quad (3.10)$$

Where $R_{equv.brick}$ is the R-value of the equivalent brick veneer and $R_{equv.insulation_{CMU}}$ is the R-value of the equivalent insulation-CMU layer.

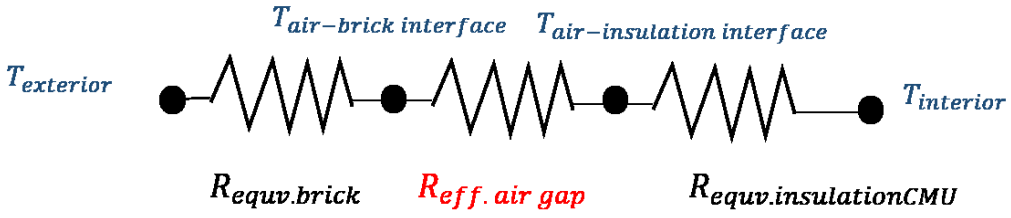

Figure 3.15: Schematic of the thermal resistance of the model in Method I.

The second method (Method II) was used to calculate the $R_{eff.air\ gap}$ value with the data in the fluent model solution by Eq. (3.11). After the iterations were completed, another Fluent model was used to determine the area-weighted average temperature of the two surfaces of the air gap and the thermal resistance value was calculated using Eq. (3.1). The q used in the equation is the average heat flux value on the interface of the air gap and insulation (e.g., the warm side of the air gap). The average heat flux value through the brick veneer was used (i.e., the cold side of the air gap) as the heat flux value q in the equation cannot be obtained as the expected equivalent thermal resistance of the air gap, $R_{eff.air\ gap}$. The $R_{air\ gap}$ shown in Figure 3.14 is obtained. $R_{air\ gap}$ doesn't consider the effect of the heat carried away by the air from vents, so the $R_{air\ gap}$ value can not be fully equivalent to the thermal performance of the air gap.

$$R_{eff.air\ gap} = \frac{\Delta T}{q} - R_{equv.brick} \tag{3.11}$$

3.2 Steady-State Thermal Models for Parametric Analysis of Different Configurations

With the air gap thermal resistance determined, steady-state thermal analysis was used to perform parametric analysis on the design of masonry ties. Although 3D thermal analysis is required to solve the point thermal bridging problem, such as tie problems in the wall assembly, the difference of R_{eff} between different configurations (ΔR_{eff}) is still the most efficient value to represent the thermal impact of the tie on the wall. Therefore, the models in this section were modelling as 3D heat transfer through wall assembly from the indoor to the outdoor. Conductive, convective, and radiation heat transport should be considered within each wall system.

Four groups of models learned in this section were solved by steady-state thermal modelling since the R_{eff} value of the air gap had been obtained from the preceding section. The air gap was set as a solid component that had the equivalent R_{eff} value of the air gap. Therefore, only conductive heat transfer occurs in the modelling. Four groups of parametric analysis are discussed in this section: (1) different tie material, (2) different tie shapes, (3) different tie spacing, and (4) different

grout condition in CMU backup wall. Based on the parametric analysis, improvement to reduce the impact of the tie on the thermal performance of the wall was discussed.

3.2.1 Physical Details of the Models

Small-size models are able to perform the parametric analysis on different configurations. The 'small size' was determined by the tie spacing defined by centreline between ties in the wall. According to the masonry design requirement, the maximum horizontal tie spacing is 800 mm, while the maximum vertical spacing is 600 mm, and the common tie spacing in construction is 400 mm × 400 mm (Hatzinikolas et al., 2015). The model with a cross-section area of 400 mm × 400 mm was considered to be the base model. The size of the brick unit was 190 mm × 90 mm × 57 mm, while the CMU block was standard block (390 mm × 190 mm × 190 mm). An adjustable rigid tie type with wire component for brick wythe was placed at the centre of the wall assembly and its material was galvanized steel, which is the most commonly used in Canada. When R15 insulation was placed in the wall, this model was named UG15 ('U' stands for the 400 mm × 400 mm unit model, 'G' represents a galvanized tie is used in the model, and '15' is the exterior insulation level used in the model). The geometry of the UG15 is shown in Figure 3.16. The models included the effect of mortar and surface air film resistance. The position of each component is presented in Figure 3.17 and Figure 3.18. Different colours in the illustration represent individual bodies in the wall assembly.

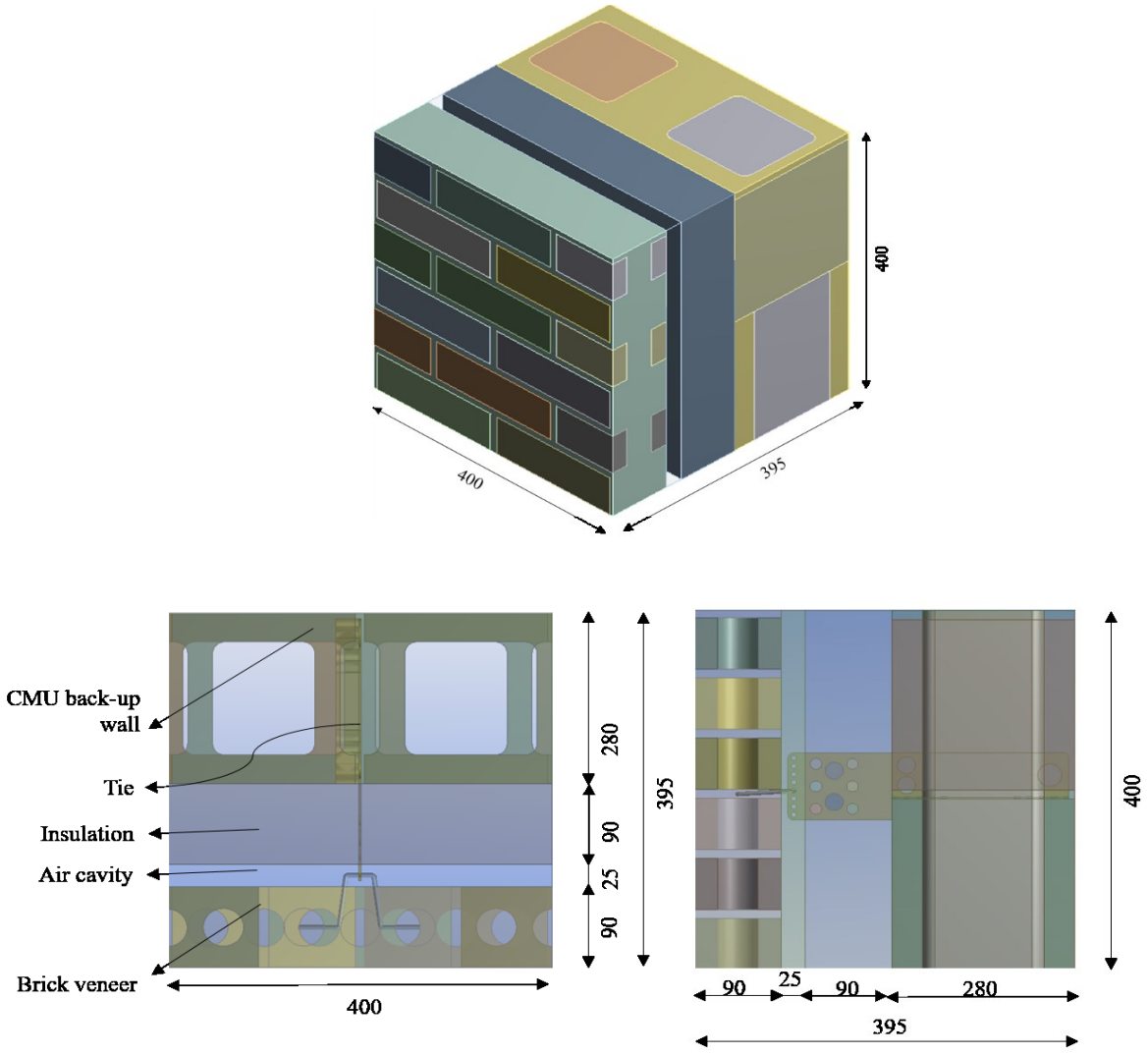

Figure 3.16: The geometry of UG15 (mm).

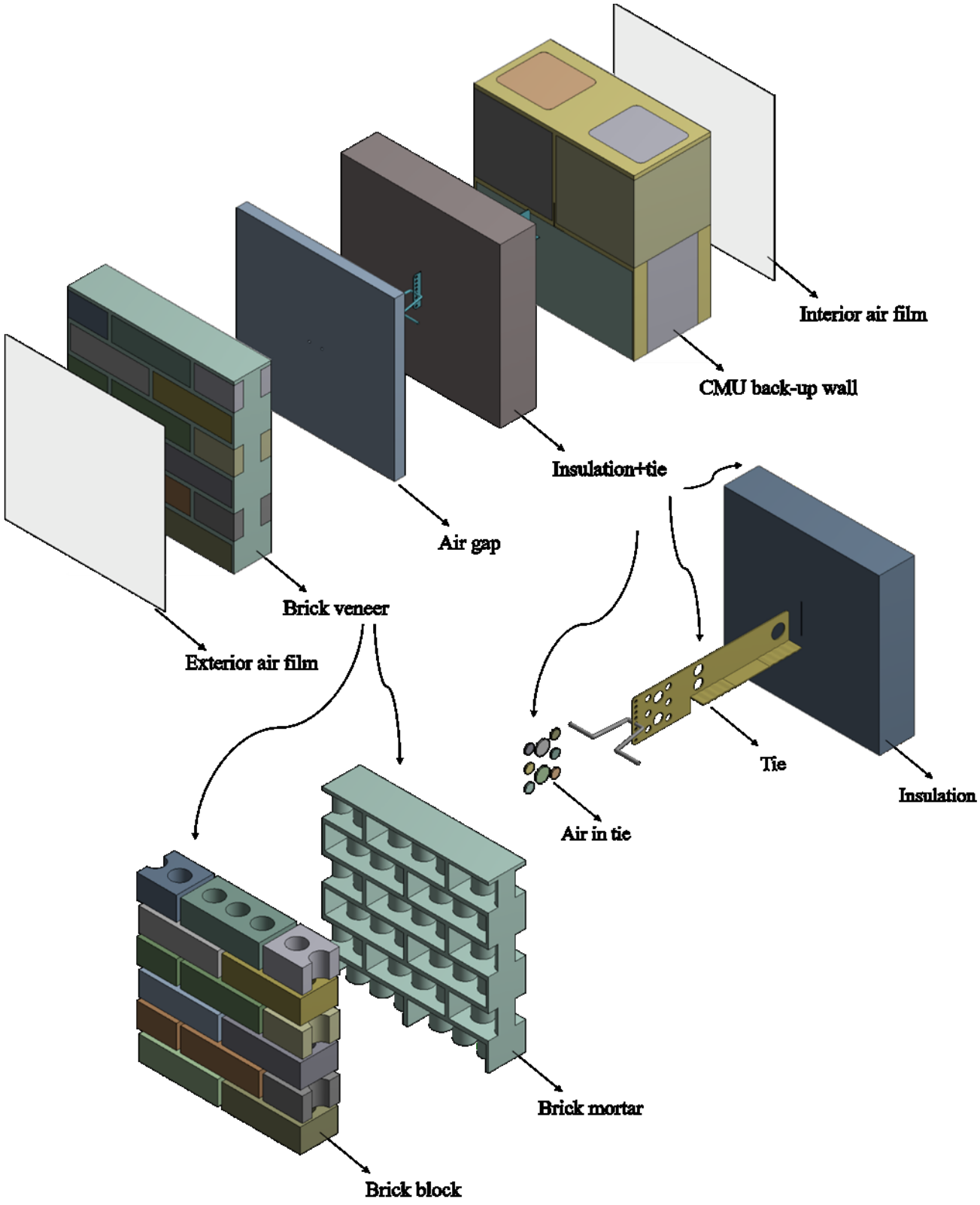

Figure 3.17: The components in the wall assembly.

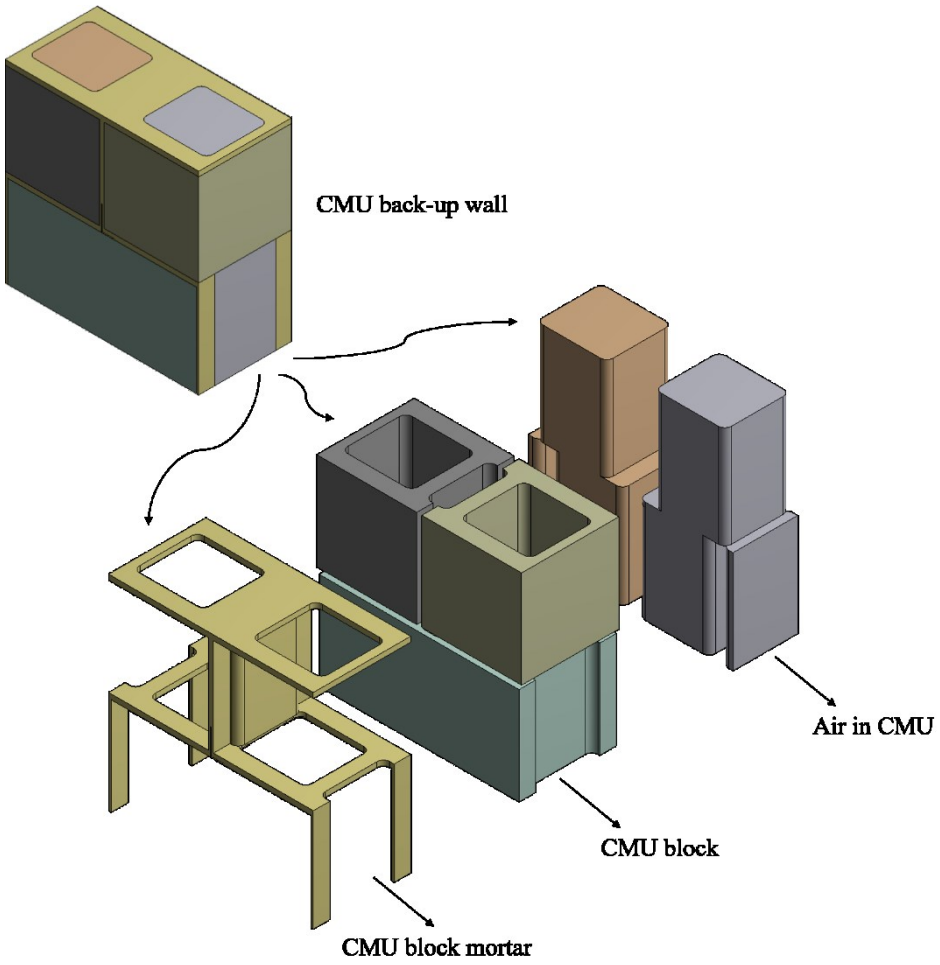

Figure 3.18: Components in CMU backup wall.

Two temperature boundary conditions were applied to the interior surface and external surface of the wall assembly to generate the heat flow through the wall. The indoor temperature was 21℃ and the outdoor temperature was -18℃, while other surfaces were adiabatic. Boundary conditions are shown in the Figure 3.19.

Thermal contact resistances were also set in the models. The values at different interfaces, listed in Table 3.3, were researched and summarized in ASHRAE 1365-RP (Roppel et al., 2012). The interfaces applying the contact resistance are indicated in Figure 3.20 and Figure 3.21.

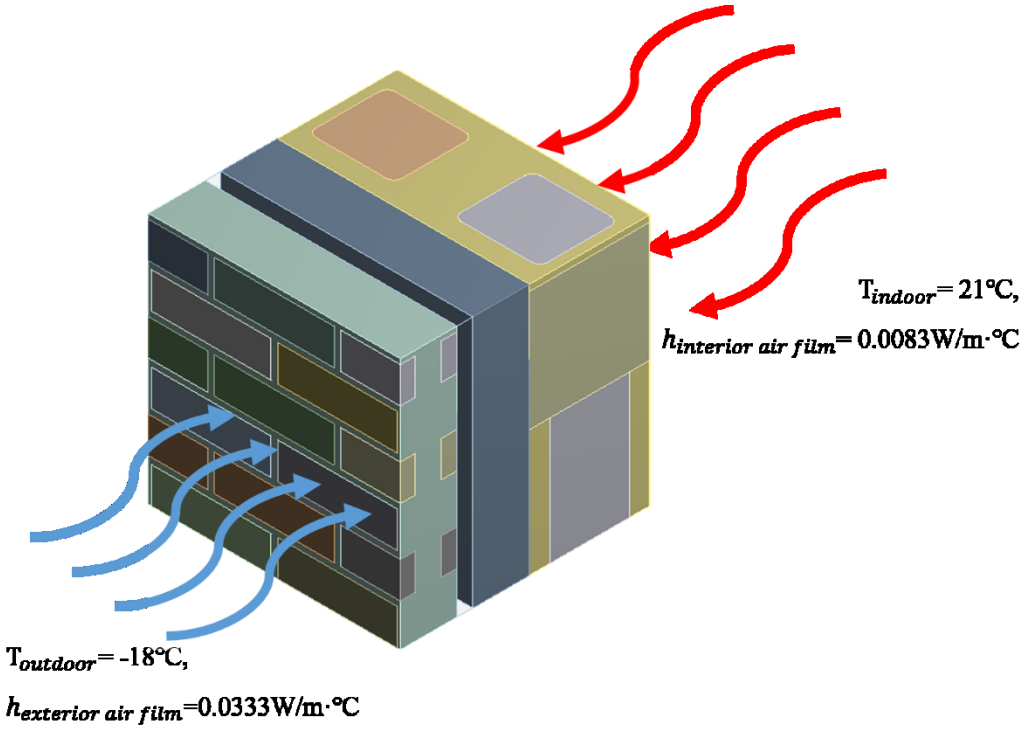

Figure 3.19: Boundary conditions in steady-state thermal models.

Table 3.3: Contact resistances at different interfaces

Location	ID	Contact Resistance (m^2·K/W)
Insulation interfaces	R_{ii}	0.010
Steel to concrete interfaces	R_{sc}	0.010
Steel to steel interfaces	R_{ss}	0.0020

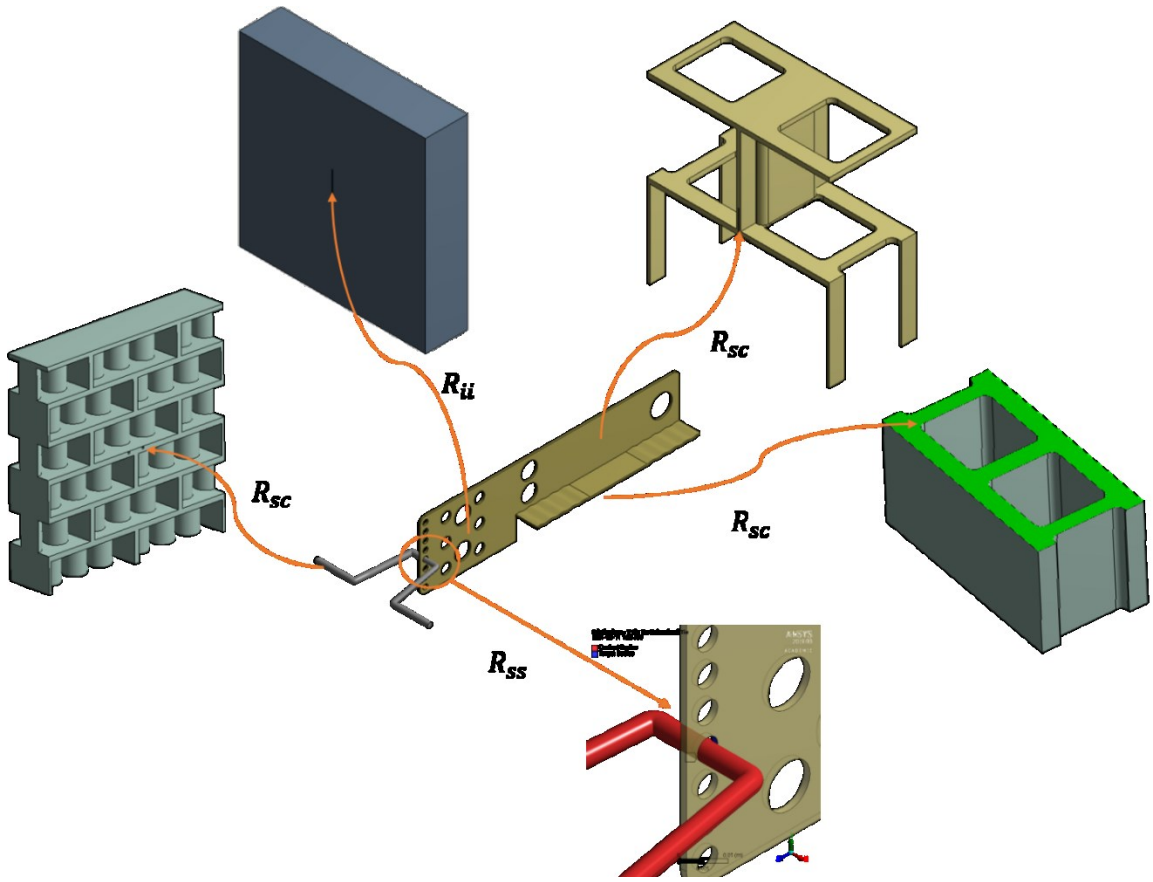

Figure 3.20: Types and position of the contact resistance around the tie.

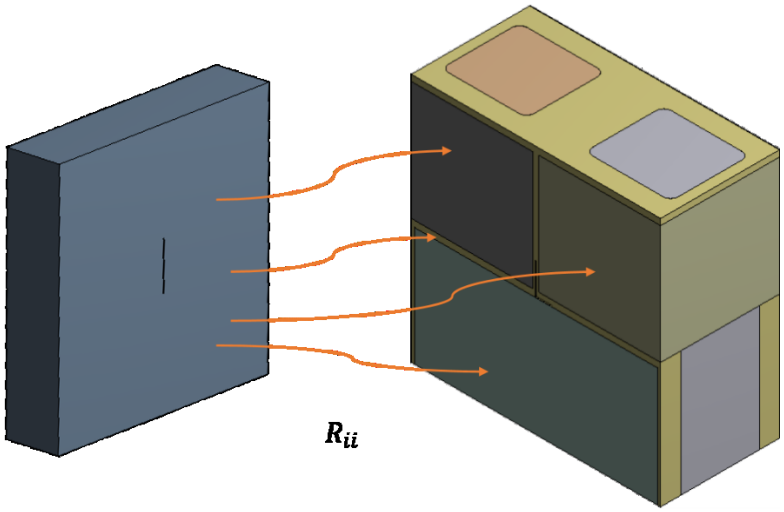

Figure 3.21: Contact resistance between insulation and CMU backup wall.

3.2.2 Parametric Analysis

The model UG15 was considered to be the base model to compare and estimate the effect of the tie on the overall thermal resistance for different cases. Due to the cold climate in Canada, the exterior insulation in the wall assembly is considered from R15 and above. In the first comparison, two different grouted conditions models were discussed. The first condition was the empty CMU backup wall model UG15, while the second was the fully grouted model UG15_FG.

The second group of discussion is the different material of tie and different insulation's R-values in the wall. The high conductivity of the tie material is the key factor that generates the thermal bridging inside the wall assembly. Essentially, changing the thermal conductivity can effectively eliminate the thermal bridging in the wall and improve the thermal performance of the wall assembly. The specimen ID representing different tie materials in the wall assembly is presented in Table 3.4. For the no-tie cases (UN models), the effective thermal resistance of the air gap should be used as the value only considering the ventilation impact. However, for the comparison purpose, the effective thermal resistance of the air gap in the UN models still used the $R_{eff.air\ gap}$ obtained from the air gap models in the last step, which include the influence of both ventilation and thermal bridging.

Table 3.4: Specimen ID of the models with different tie material

Specimen Size		0.4 m × 0.4 m (unit specimen)			
Tie Cases		No-tie	Galvanized steel tie	Stainless tie	GFRP tie
Nominal R-value of Insulation	R15	UN15	UG15	US15	UF15
	R20	UN20	UG20	US20	UF20
	R25	UN25	UG25	US25	UF25

Note:

First character: 'U' represents unit cases for one tie studies, 0.4 m × 0.4 m.

Second character: Tie with different material ('N' for no-tie; 'G' represents galvanized steel tie; 'S' represents stainless steel tie; 'F' represent GFRP tie).

Figures: R-value of the solid insulation in the wall assembly (ft2·°F·h/BTU).

In addition to changing the tie material, the other three groups of specimens were discussed to learn the thermal impact of different tie design. In the first group, three models with different tie

shape designs were studied, as shown in Figure 3.22. To ensure that the different ties have the same adhesion with mortar, three ties considered in this study (UG15, UG15_D170, and UG15_D150) had the same surface area. To eliminate the impact of the holes on the tie body, each of the three models had two 19-mm diameter holes and one 25-mm diameter hole, which were equidistant from their adjacent edges. As each tie shape was changed by adjusting the tie length in the CMU backup wall, the influence factor can also be considered as the depth of the tie in the CMU wall.

The slotted tie used in UG15 is one of the most common shapes of ties used in Alberta. The type of ties used in the models discussing the tie spacing, grouted condition, and the thermal breaks were the tie with dimensions (184 × (50 + 25)) mm, as shown in the case of UG15 in Figure 3.22.

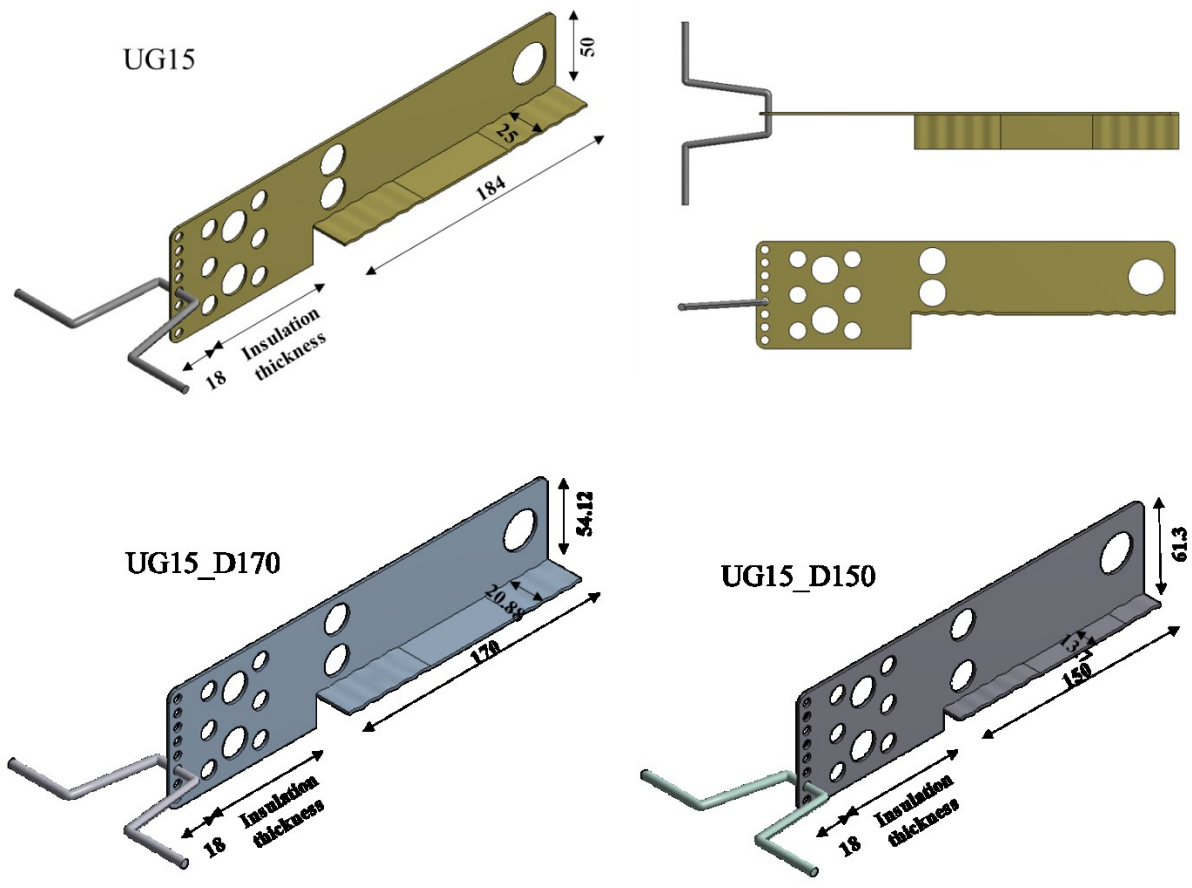

Figure 3.22: Ties with different depth (mm).

In the second group, three models were built to discuss the thermal properties of walls with different tie spacing. The requirements of horizontal tie spacing and vertical tie spacing are different due to the structural designs. However, in terms of heat transfer, the spacing in different directions only affect the unit area of one controlled tie. Therefore, only the horizontal spacing was changed to vary the unit area of each tie case. As the maximum horizontal tie spacing is 800 mm, three models with a horizontal dimension varying from 400 mm, 600 mm, and 800 mm were set up. The models with different tie spacing typically used in the assemblies in construction (centreline dimensions) are shown in Figure 3.23.

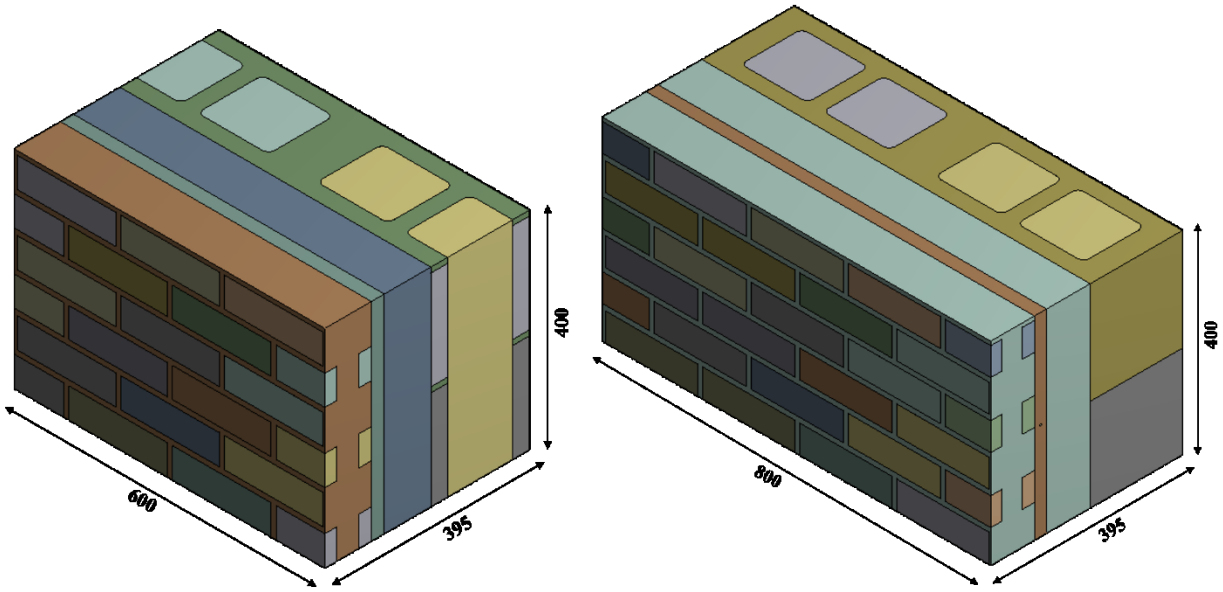

Figure 3.23: Models with different tie spacing (mm).

To reduce the thermal bridging effect of the metal tie in the wall assembly, a thermal break was added around the tie body in the last group. Two models were studied to show the effect of using thermal breakers at the edges of the tie by using whole-length tie insulation. The thickness of the thermal break of the first model was 2.3 mm on each side, except at the tie end, which was 6 mm. To determine the range of the R_{eff} value that can be improved by the thermal break, the other model with 4.2 mm thermal break on each side, which fully filled the mortar joint width (10 mm), was also set up and solved. The configurations of the thermal breakers are shown in Figure 3.24.

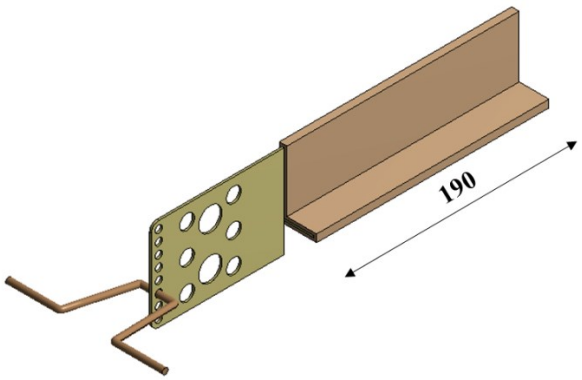

Figure 3.24: Thermal breaking configuration of whole tie insulation (mm).

All tie design differences and different wall configurations used in this study are listed in Table 3.5 as well as the different variables considered in each model.

Table 3.5: Specimen ID for different tie design (all cases based on UG15)

Parameters	ID	Descriptions
Ties depth in the backup wall	UG15	(184 × (50 + 25)) mm
	UG15_D170	(170 × (54.12 + 20.88)) mm
	UG15_D150	(150 × (61.3 + 13.7)) mm
Tie spacing	UG15	400 (H) × 400 (V)
	UG15_S64	600 (H) × 400 (V)
	UG15_S84	800 (H) × 400 (V)
Thermal breaks configurations	UG15	No thermal breaking
	UIG15_F	with full length insulation (2.3 mm thickness on each side)
	UIG15_F_10mm	Tie with full length and maximum thickness tie insulation (4.2mm thickness on each side)
Grouted condition in CMU backup wall	UG15	Empty
	UG15_FG	Fully grouted

Note:

First character: 'U' represents unit cases for one tie studies, 0.4 m × 0.4 m.

Second character: Tie with different material ('G' represents galvanized steel tie; 'IG' represents Galvanized steel tie with thermal break around the tie).

Figures after tie types: R-value of the exterior insulation in the wall assembly (ft2·°F·h/BTU).

Characters after the "_": D represents the depth of tie in the CMU, the figures are the depth values in the CMU; S represents the spacing of the tie in the masonry wall, the former figures are the horizontal spacing, while the latter figures are the vertical spacing; 'FG' represents the fully grouted model.

Thermal data for various material are provided in

Table 3.6. The effective R-value of the empty CMU block and the grouted CMU block are 0.23 m^2·K/W and 0.168 m^2·K/W, respectively, calculated based on previous studies (ASHRAE, 2017b; Cavanaugh and Speck, 2002; NECB, 2017). In the numerical modelling, the CMU block and the air in the voids are treated as the same solid material to equate the total R-value of the two types of components to the reported effective R. In other words, the k value of the blocks and the air was changed to an equivalent k value. This equivalent method was also the same for the grouted CMU block. The thermal conductivity of the two types of block can be obtained by Eq. (3.8). The corresponding thermal conductivity of two types of CMU block are 0.87 W/m·K and 1.13 W/m·K.

Table 3.6: Material properties of wall assemblies

Components	Thermal Conductivity k (W/m·K)	Density ρ (kg/m^3)	Specific Heat Capacity c (J/kg·K)	Thickness t (mm)	Emissivity ε
Exterior air film	0.0333			1	
brick	0.78			90	0.93
Cement mortar	0.5			-	
Air gap	0.3571			25	
Mineral wool board	0.034	70	840	90 (R15)	0.855

Masonry tie (Stainless steel)	17	8060	530	1.59 (16 gauge)	
Masonry tie (Galvanized)	62	7800	470	1.61 (16 gauge)	0.6
Masonry tie (GFRP)	0.2			1.61 (16 gauge)	
Empty CMU block	0.87	1800		190	0.855
Fully grouted CMU block	1.13			190	
Air	0.026	1.1614	1007		
Interior air film	0.00833			1	

4 Results and Discussion

This chapter presents the results and discussions of the data obtained from the finite element modelling of the air gap analysis. The results of the parametric analysis, investigation of the influencing factors affecting the tie's thermal bridging effect on the effective walls' thermal resistance (e.g., material, depth, spacing, and adding thermal breaks) are also discussed. In addition, improvement strategies are suggested to reduce the tie's thermal bridging effects and enhance the thermal resistance of the wall.

4.1 R-value of the Air Gap

The equivalent thermal resistances of the brick veneer and insulation-CMU-backup-wall layer were obtained to provide the components' thermal properties used in the air gap models as described in Section 3.1.2. The effective thermal resistance of two equivalent layers, brick veneer layer and insulation-CMU-backup-wall layer, was solved using steady-state thermal modelling. The resultant thermal properties of the equivalent layers for Group 1 WG (whole wall with galvanized steel ties) models with different insulation boards are presented in Table 4.1.

Table 4.1: Thermal properties of two equivalent bulk layers in different WG cases

Location		Thickness (m)	Heat Flux (W/m^2)	Thermal Resistance ($m^2 \cdot K/W$)	Thermal Resistance (including air film) R_{total} ($m^2 \cdot K/W$)	Thermal Conductivity ($W/m \cdot K$)	Sum of Two Equivalent Layers $R_{equv.sum}$[1] ($m^2 \cdot K/W$)
Equivalent Brick Veneer		0.09	284.49	0.14	0.17	0.54	
Combined Insulation and CMU	R5	0.22	33.70	1.16	1.28	0.17	1.44
	R10	0.25	23.34	1.67	1.79	0.14	1.96
	R15	0.28	18.62	2.10	2.22	0.13	2.38
	R20	0.31	15.30	2.55	2.67	0.12	2.84
	R25	0.34	13.08	2.98	3.10	0.11	3.27

1. $R_{equv.sum}$ is the sum of the thermal resistance of the equivalent brick veneer and the equivalent insulation-CMU layer.

The temperature distribution in the air gap is presented in Figure 4.1. Due to the limitation of updating the temperature distribution after each simulation, the average heat flux value on the interior surface is used as a convergence check in the iteration process. Table 4.2 shows the heat flux values of the two types of models in each iteration and the R_{eff} value of the WG15 model. The results show that in the case of WG15, the model converged in six iterations and it was inferred that all calculations for different configurations can be converged within six iterations.

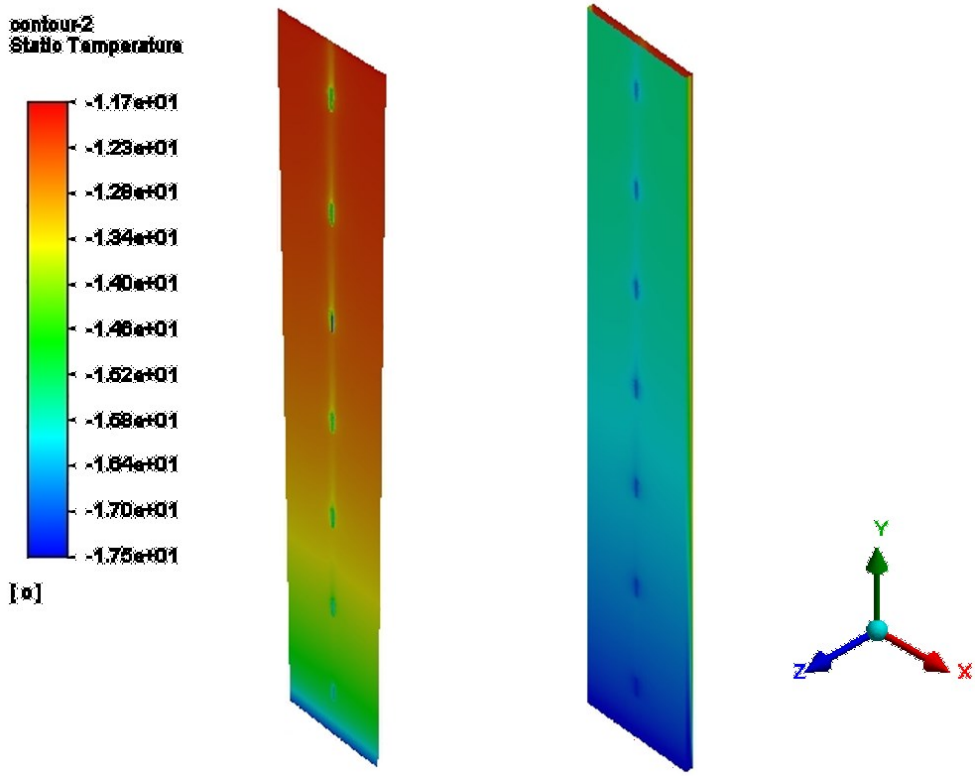

(a) (b)

Figure 4.1: Temperature distribution on the air gap's surface in the WG15model: (a) interface of the brick veneer and air gap and (b) interface of the insulation and air gap.

Table 4.2: Results of each iteration for specimen WG15

No. of Iterations	Heat Flux Value in Fluent Model(W/m^2)	Heat Flux Value in Steady-State Model ($m^2 \cdot K/W$)	Steady-State Thermal R_{eff} ($m^2 \cdot K/W$)
1	19.83	14.01	2.78
2	14.01	15.70	2.48
3	15.70	15.54	2.51
4	15.54	15.56	2.51
5	15.56	15.56	2.51
6	15.56	15.56	2.51

In Method I, the thermal resistance of the two equivalent layers is subtracted from the total resistance of the entire assembly to calculate the resistance of the air cavity. Table 4.3 shows the results of the air gaps' effective thermal resistance, while the relationship between the effective thermal resistances of the air gap and the different exterior insulation R-values (WG models) is shown in Figure 4.2. The R-values ranges from 0.121 $m^2 \cdot K/W$ to 0.151 $m^2 \cdot K/W$ in the case of a 25-mm air gap in a wall assembly with galvanized steel ties.

Table 4.3: Results of the air gap in different WG models calculated by two methods

Cases	Results calculated by Method I				Results calculated by Method II			
	$R_{equv.sum}$ ($m^2 \cdot K/W$)	q (W/m^2)	R_{eff} ($m^2 \cdot K/W$)	$R_{eff.\ air\ gap}$ ($m^2 \cdot K/W$)	$R_{equv.brick}$ ($m^2 \cdot K/W$)	$T_{air-insulation}$ (°C)	ΔT (°C)	$R_{eff.airgap}$ ($m^2 \cdot K/W$)
WG5	1.44	24.92	1.56	0.121	0.17	-10.19	7.82	0.147
WG10	1.96	18.70	2.09	0.128	0.17	-12.10	5.90	0.149
WG15	2.38	15.56	2.51	0.124	0.17	-13.07	4.93	0.150
WG20	2.84	13.10	2.98	0.142	0.17	-13.84	4.16	0.150
WG25	3.27	11.40	3.42	0.151	0.17	-14.38	3.62	0.151

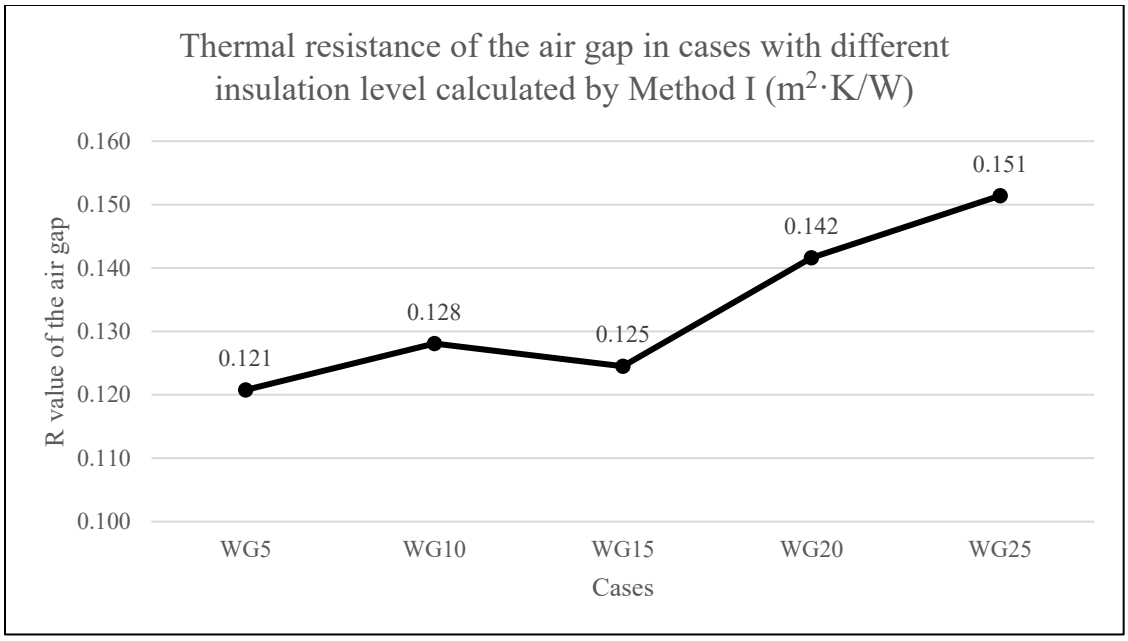

Figure 4.2: R-value of the air gap in different WG specimens calculated by Method I (m^2·K/W).

The effective thermal resistance of the air gap and its relation with different insulation R-values using models without ties (WN models) are presented in Table 4.4 and Figure 4.3. Results show that the R-value of the WN models increases linearly with the increase of the nominal exterior insulation R-value.

Table 4.4: Results of the air gap in different WN specimens calculated by two methods

	Results calculated by Method I				Results calculated by Method II			
Cases	$R_{equv.sum}$ (m^2·K/W)	q (W/m^2)	R_{eff} (m^2·K/W)	$R_{eff.\ air\ gap}$ (m^2·K/W)	$R_{equv.brick}$ (m^2·K/W)	$T_{air-insulatio}$ (°C)	ΔT (°C)	$R_{eff.airgap}$ (m^2·K/W)
WN5	1.81	19.33	2.02	0.210	0.17	-11.85	6.15	0.150
WN10	2.58	13.56	2.88	0.303	0.17	-13.66	4.34	0.152
WN15	3.34	10.44	3.73	0.394	0.17	-14.65	3.35	0.153
WN20	4.10	8.50	4.59	0.486	0.17	-15.27	2.73	0.154
WN25	4.87	7.16	5.45	0.577	0.17	-15.69	2.31	0.154

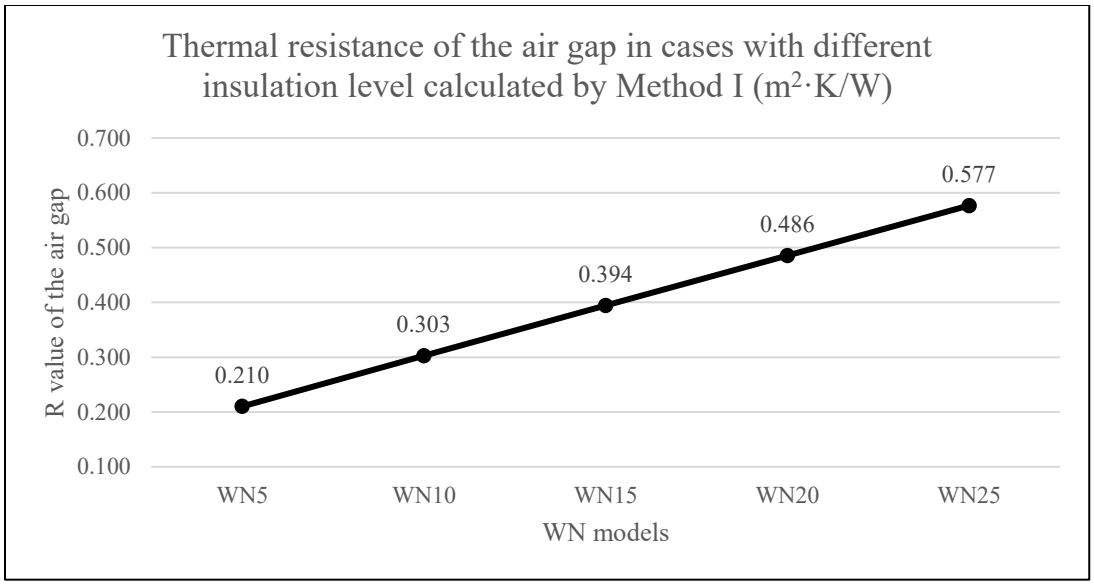

Figure 4.3: R-value of the air gap in different WN specimens calculated by Method I ($m^2 \cdot K/W$).

From Figure 4.2 and Figure 4.3, all assemblies showed a directly proportional relationship between the insulation R-value and the obtained effective air gap R-value, except wall WG15, which showed a lower air gap R-value compared to wall WG10. In fact, the only difference between the WG models and WN models is that in the WG models the effective thermal resistance of each layers decrease, especially the insulation. All other components are in series to the insulation. According to the law of heat conduction (Fourier's law) shown below, the modelled results of the WG models should be in a linear fashion, similar to the results of WN models.

$$q = k \cdot (-\nabla T) \tag{3.12}$$

where ∇T is the temperature gradient in all direction.

Therefore, the air gap R-value for WG15 was considered an erroneous result and the corrected effective thermal resistance of the air gap in model WG15 was estimated to be 0.135 m^2K/W using the linear function presented in Figure 4.4. Due to the cold climate condition in Canada, insulation above R15 is required in construction.

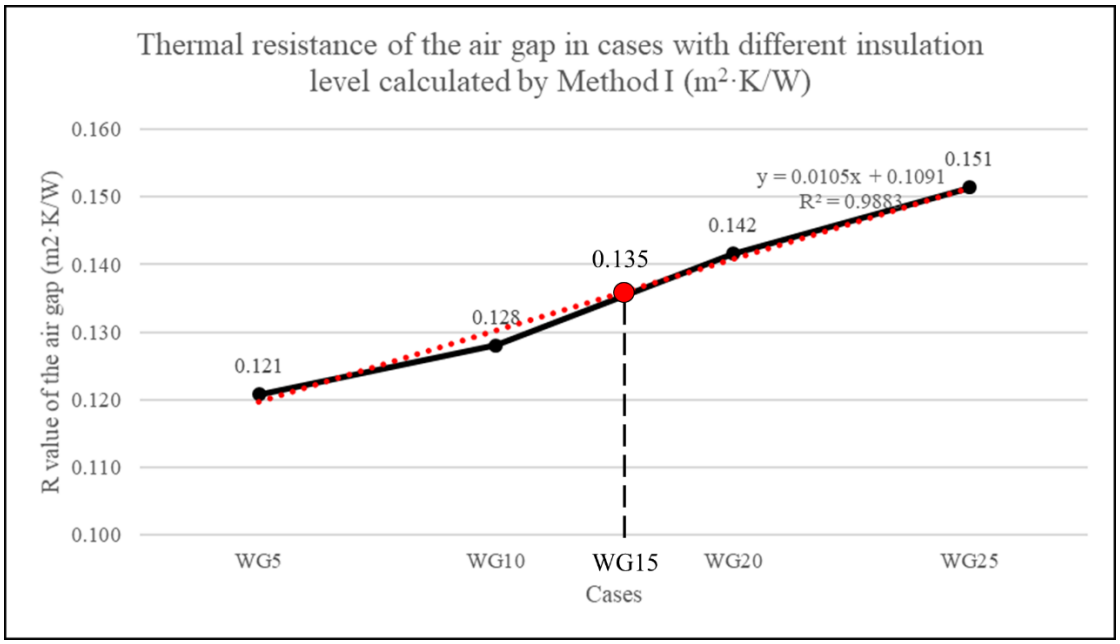

Figure 4.4: R-value of the air gap in different WG specimens calculated by Method I (removed error value and determined new WG15 value) (m^2·K/W).

Figure 4.5 presents the relationship for the thermal resistances of the air gap in the WG and WN models. The ΔR_{eff} between the two models increases as the nominal exterior insulation R-value increases, which suggests that the thermal impact of metal ties on the assembly increases when the exterior insulation level increases. Therefore, it can be concluded that metal ties have a significant effect on the thermal performance of the air gap in the wall assembly.

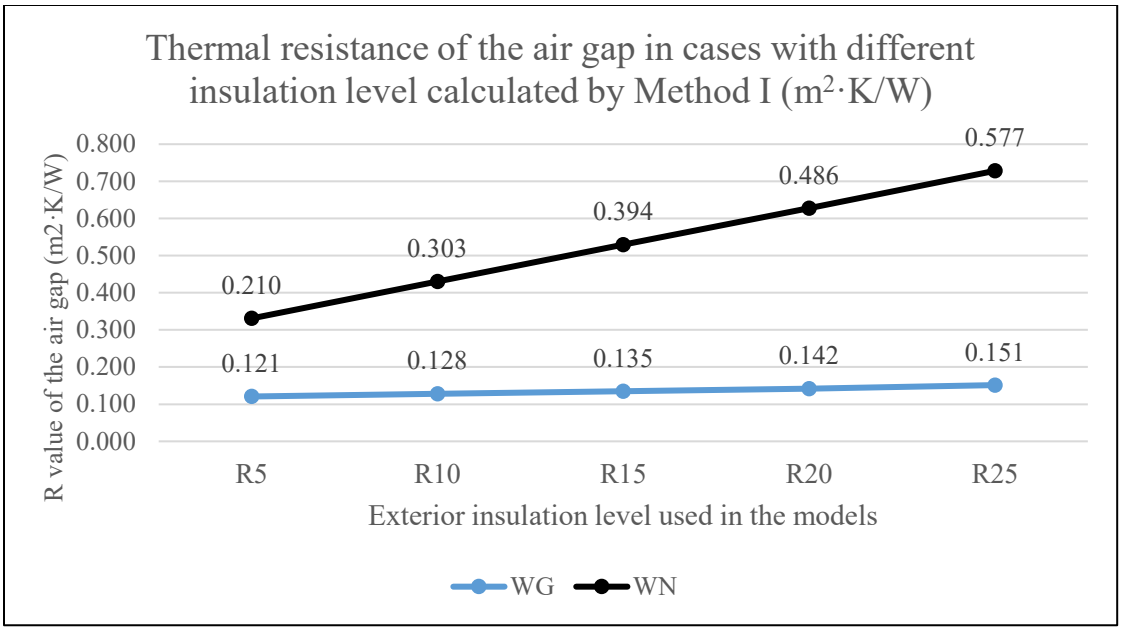

Figure 4.5: Corrected thermal resistance of the air gap in different models calculated by Method I (m^2·K/W).

The schematic of the heat transfer path through the wall assembly is shown in Figure 3.1(b), while the heat transfer rates through each path are presented in Table 4.5. As the air velocity entering the air gap is fixed, the heat loss from the air inlet or the heat input with air flow Q_2 is also fixed. The net heat loss carried by the air flow is the sum of the heat loss through the air inlet and air outlet, which is labelled as $(Q_2 + Q_3)$. With the increase in insulation level, the temperature of the air gap drops and the absolute value of $(Q_2 + Q_3)$ decreases gradually. However, in the case of a fixed temperature difference between the assembly at 39 K and fixed air velocity at 0.1 m/s through the air gap, the percentage of the net heat loss carried by the airflow to total heat input ($(Q_2 + Q_3)/Q_{total}$) is stable around 28.5% when the R-value of the exterior insulation is varied. By comparing models with different air velocities, results show that faster air carries more heat loss.

Table 4.5: Total heat transfer rate through the air gap's inlet and outlet

Model IDs	Q_1 Total heat transfer rate through the exterior surface (W)	Q_2 Total heat transfer rate through the air inlet (W)	Q_3 Total heat transfer rate through the air outlet (W)	$Q_2 + Q_3$ Net heat loss through the air vent (W)	Q_{total} Total heat transfer rate through the interior surface (W)	$\frac{Q_2 + Q_3}{Q_{total}}$ Percentage of heat loss through the air (%)
WG5	-19.94	-53.08	45.13	-7.95	27.90	28.50%
WG10	-14.91	-53.06	47.06	-6.00	20.94	28.64%
WG15	-12.42	-53.05	48.08	-4.97	17.43	28.54%
WG20	-10.45	-53.05	48.83	-4.22	14.67	28.77%
WG25	-9.09	-53.05	49.36	-3.69	12.77	28.90%
WG15_V0.05	-14.56	-26.56	23.86	-2.70	17.25	15.62%
WG15	-12.42	-53.05	48.08	-4.97	17.43	28.54%
WG15_V0.15	-10.84	-79.56	72.87	-6.68	17.56	38.06%

Note:

1. A positive sign indicates heat flow into the wall system, while a negative sign indicates heat flow out the wall.

The R-values of the air gap calculated by Method II in each wall assembly are presented in Table 4.6, while the relationship between the R-value of the air gap and insulation is shown in Figure 4.6. The average R-value of the air gap within the WG walls with different insulation levels is approximately 0.150 $m^2 \cdot K/W$. Similar to Method I for WG 15, results show that the R-value increases with an increase in the exterior thermal insulation R-value. The average difference in R-values between the two models is 0.0035 $m^2 \cdot K/W$, which indicates the metal ties have an insignificant impact on the R-value of the air gap in the wall assembly, contradicting the results from Method I. Further investigation on the discrepancies between the two methods is needed in future studies. Therefore, the R-value of the air gap with uniformly spaced metal ties is almost stable at 0.150 $m^2 \cdot K/W$ using any level of exterior insulation board in the Method II calculation.

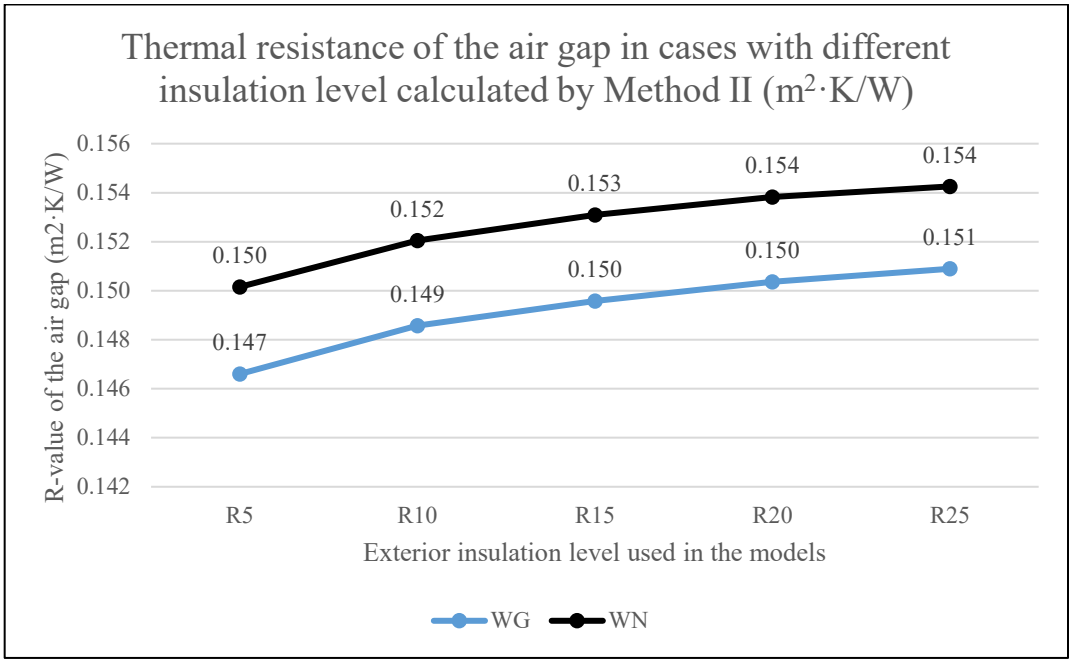

Figure 4.6: R-value of the air gap in WG and WN specimens calculated by Method II (m^2·K/W).

The $R_{eff.airgap}$ results using different air velocities are shown in Table 4.6 and Figure 4.7. Figure 4.7 presents the R-values obtained by Method I and II in the case of 0.05 m/s, 0.1 m/s and 0.15 m/s air gap velocities. Results show that faster air velocity causes more heat loss through the air gap (Table 4.5), which will reduce the thermal performance of the air gap and reduce the R_{eff} value of the wall assembly. In Method I, the 0.05 m/s increase in air velocity of the air gap causes a 0.02 m^2·K/W to 0.025 m^2·K/W decrease in the air gap's R-value. A 15% to 20% change of the air gap's R-value caused by air gap velocity only affected 1% of the wall assemblies' R_{eff} value. Therefore, the air velocity does not have a significant impact on the thermal resistance of the entire wall assembly if the air gap velocity is within 0.05 m/s to 0.15 m/s and the effective thermal resistance of the air gap can be determined based on only the insulation R-value, which was confirmed with Method II as well. Consequently, the R-value of the air gap for Model I is the corrected value of the model WG15 (0.135 m^2·K/W), while the $R_{eff.air\ gap}$ value is 0.150 m^2·K/W when metal ties are evenly spaced in the specimen for Method II.

Table 4.6: Results of the air gap with different air velocities calculated by two methods

Cases	Method I Results				Method II Results			
	$R_{equv.sum}$ (m^2·K/W)	q (W/m^2)	R_{eff} (m^2·K/W)	$R_{eff.\ air\ gap}$ (m^2·K/W)	$R_{equv.brick}$ (m^2·K/W)	$T_{air-insulation}$ (°C)	ΔT (°C)	$R_{eff.airgap}$ (m^2·K/W)
WG15_V0.05	2.38	15.40	2.53	0.150	0.167	-12.54	5.46	0.188
WG15	2.38	15.56	2.51	0.124	0.167	-13.07	4.93	0.150
WG15_V0.15	2.38	15.68	2.49	0.106	0.167	-13.60	4.40	0.114

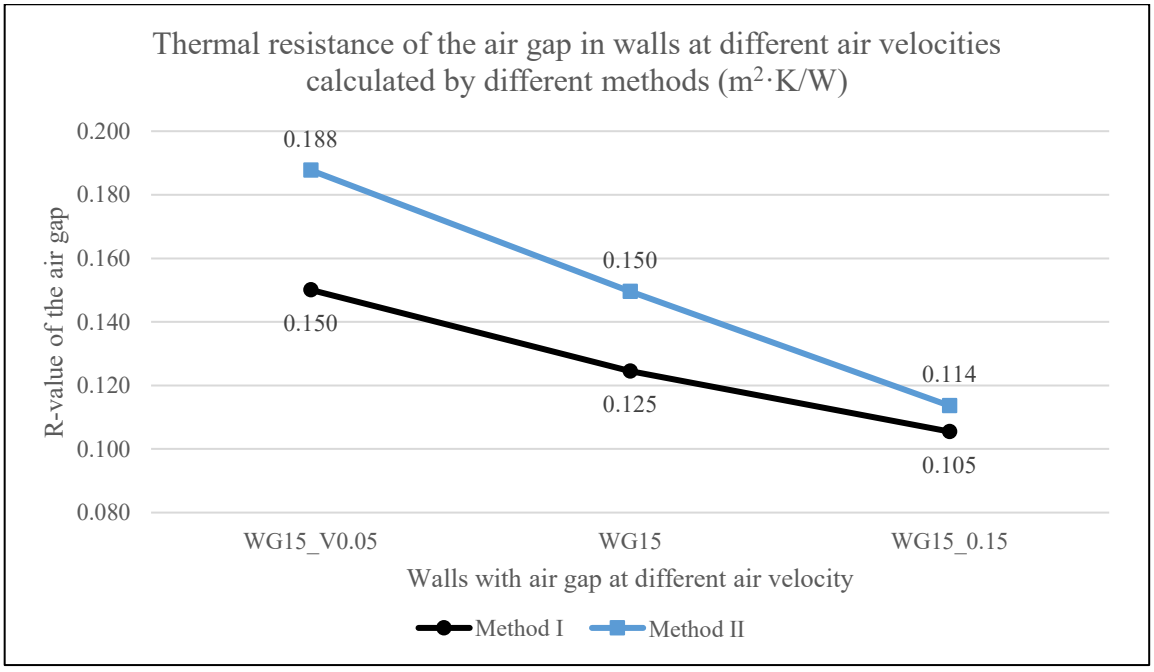

Figure 4.7: R-values of the air gap with different air velocity calculated by different methods.

The behaviour of the $R_{eff.air\ gap}$ of different masonry wall models was found to be comparable. Higher exterior insulation levels could increase the effective thermal resistance of the air gap, while faster air velocity decreases the effective thermal resistance of the air gap. But when refining

the exterior insulation R-value in the models, the results obtained from Method I have a linear increase while the results from Method II show minimal improvement. The calculation in Method I is reasonable and the usual method used to obtain an effective and equivalent value of a component in the wall assembly. Method II has the advantage of reducing the number of accumulated errors resulting from the process of adding and subtracting equivalent results. However, the drawback of Method II is the area-weighted average heat flux value through the insulation-air gap interface that may not precisely consider the heat flux value of the ties. The heat flux values on the ties cross-section can be extremely high and can cause significant errors in the calculation process. Therefore, the effective thermal resistance of the air gap is determined as the $R_{eff.air\ gap}$ obtained from Method I. Considering the commonly used exterior wall insulation in practice are R15 and higher, the effective thermal resistance of the air gap is considered similar to the value obtained for WG15 (0.135 $m^2 \cdot K/W$).

The resulting air gap's effective thermal resistance, includes the impact of ventilation in the air gap and tie's thermal bridging, and the comparisons in Figure 4.7 show the necessity of the $R_{eff.air\ gap}$ calculation. Figure 4.7 shows the thermal resistance of a vertical air gap in different references and the reduction percentage of the obtained $R_{eff.air\ gap}$ compared to the thermal resistance of the air gap selected from various resources. The reductions indicate the ventilation in the air gap and the tie's thermal bridging effect can cause a minimum 15.6% decrease in the effective R-value of the air gap, and a maximum biggest reduction of 47.2%. Therefore, obtaining a new and accurate value for the thermal resistance of the air gap rather than selecting an existing value from the available codes is necessary.

Table 4.7: Comparisons between the obtained $R_{eff.air\ gap}$ and the thermal resistance of the air gap selected from various resources

Thermal resistance of a vertical air gap ($(m^2 \cdot K)/W$)	Reference	Reduction of $R_{eff.air\ gap}$ caused by ventilation and thermal bridging effect (%)
0.135	-	-
0.18	25-mm unventilated air gap[1] ISO 6946 (2017)	25%

0.22	20-mm air gap ASHRAE (2017)	47.2%
0.16	25-mm air gap Morrison Hershfield (2018)	15.6%
0.17	20-mm to 50-mm air gap CLEAR[2]	20.6%

Note: 1. In ISO 6946 (2017), a 25-mm air gap with small ventilation openings (e.g., weep holes on the brick veneer can be seen as an unventilated air gap)

2. CLEAR: Comfortable Low Energy Architecture, a multimedia teaching package meets European and South Asia architecture requirement.

4.2 Parametric Analysis of Influencing Factors of the Tie design to Affect the Thermal Properties of the Wall Assembly

Five parameters were addressed to determine the thermal bridging effect of ties on the overall thermal resistance of cavity masonry walls:

- CMU backup wall type (fully grouted and un-grouted);
- Tie material (galvanized steel, stainless steel, and GFRP) and insulation R-values (R15-R25);
- Tie depth as described in Table 3.5;
- Tie spacing (400 mm, 600 mm, and 800 mm on centre);
- Suggested schemes introducing ties covering insulation.

Thermal bridging caused by the presence of insulation penetrations, such as ties, reduces the effective thermal resistance of concrete masonry walls largely. Therefore, in addition to comparing and addressing the above parameters, the results are compared with no-tie walls, as described previously in Table 3.4.

4.2.1 Grout Conditions in CMU Backup Wall

Thermal resistance and heat flux values of model UG15 (no grout in CMU) and UG15_FG (fully grouted) are shown in Table 4.8. A comparison between these two cases was performed and the percentage difference in the thermal resistance for the two cases was determined (Table 4.8). A slight reduction of 1.4% in the R_{eff} value was observed in the case of fully grouted wall compared to that of an empty backup wall assembly. For validation, the results were compared to literature

data obtained from the thermal catalog (National Concrete Masonry Association, 2012). The literature data discusses the case of an 8-inch CMU masonry wall assembly with a density of 115 PCF (1842 kg/m^3). Using a 3.50-inch (89-mm) insulation board, an R-value reduction of 0.9% to 1.8% was observed depending on the insulation used in the wall. Based on the finite element simulation results and literature data, it was concluded that the presence of grout has an insignificant effect on the wall‘s effective thermal resistance. Therefore, the CMU backup walls were all considered to be un-grouted walls in this study. Figure 4.8 shows the finite element simulation results of the heat flux distribution on the interior surface for walls with different grout conditions.

Three modelling methods were used to simulate the CMU cores for the two assemblies (UG15 and UG15_FG). First, CMU cores are simulated and modelled as solid parts with equivalent thermal conductivity of the CMU backup wall for the UG15. Another method of the simulation was applied by modelling the CMU core as air while considering the convection and radiation effects, labelled as UG15_c, with the average convective coefficient selected from the simulation results by Henrique Dos Santos et al. (2017). In Henrique's study, they simulated different shapes of hollow CMU blocks and obtained the average convective coefficient in the CM cores in different temperature differential conditions. Based on the average temperature difference of the CMU block around 10 K, for 8-inch two-cores CMU blocks, the average convective heat transfer coefficient was 1.85 W/m^2·K. Table 4.8 shows the results of both modelling strategies. The results showed a significant impact of the modelling strategy on the effective thermal resistance. When the convection and radiation effects were considered, the effective thermal resistance of the wall increased by 17.1% compared to the equivalent thermal conductivity method. Therefore, CMU core modelling strategies are considered an essential factor to calculating the effective thermal resistance. However, the limitation of the third approach, which considers air convection and radiation in the cores, is that the convective and radiative coefficients are temperature dependent, resulting in a significant effect on the models' solution. The average convective coefficient selected from the simulation results by Henrique Dos Santos, Fogiatto, and Mendes (2017) does not completely match the model conditions in this study and cannot accurately address the simulation. Therefore, the CMU blocks and air in the voids are simulated as an equivalent layer through all the addressed assemblies in this study.

Table 4.8: Data for different grout condition in CMU backup wall

	ΔT (K)	Heat flux value (W/m^2)	R_{eff} value ($m^2 \cdot K/W$)	Percentage change (%)
UG15 (equivalent)	39	15.46	2.52	
UG15_FG	39	15.68	2.49	-1.39%
UG15_c (air with convection)	39	13.21	2.95	17.1%

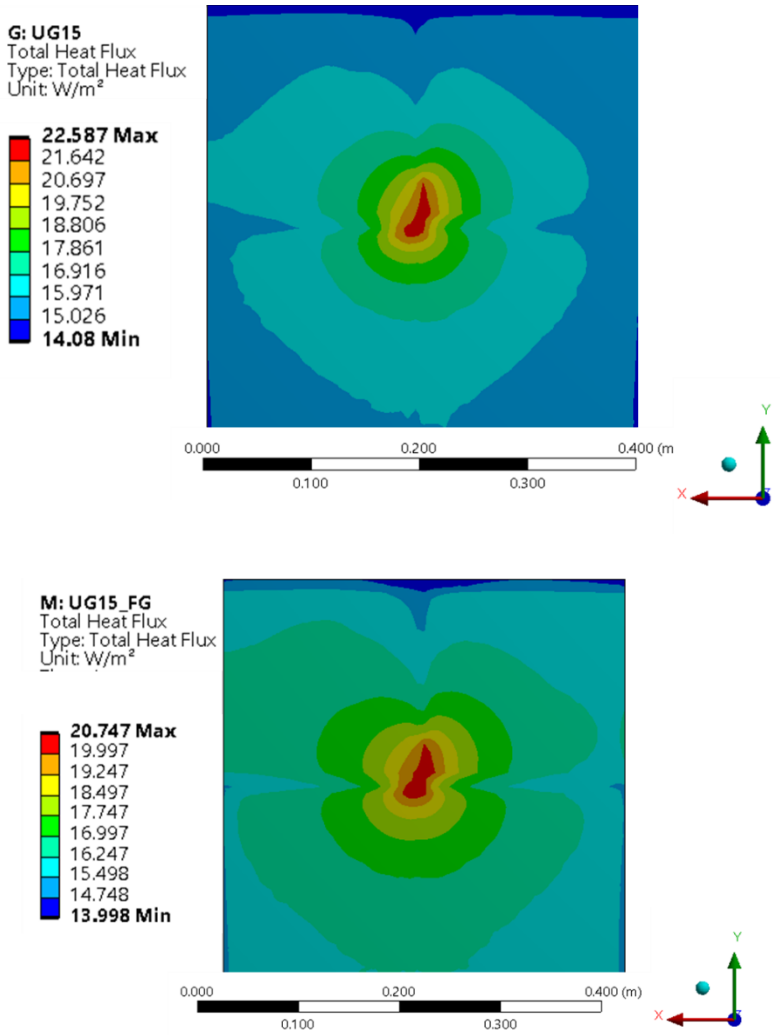

Figure 4.8: Heat flux distribution on the interior surface of concrete block backup wall with different grout conditions (W/m^2).

4.2.2 Impact of Different Tie Material and Different Insulation Cases

The R_{eff} values of the specimens with a galvanized tie, stainless tie, GFRP tie, and without a tie using different R-values of insulation boards are shown in Table 4.9. To compare the overall thermal resistance of each assembly, Figure 4.9 combines the R-values of the exterior insulation board and the R_{eff} value for each addressed assembly. No tie models (UN models) can be seen as an ideal group to present the clear wall's properties. Compared to the results of UN models, all results' differences show the thermal impact of the tie on the masonry wall assembly due to the thermal conductivity of the tie material and insulation's R-value. The comparisons intuitively demonstrate the thermal effect of changing tie material on the thermal resistance of the walls, and the improvement and reduction effect also can be presented clearly. UN models have the highest R_{eff} values of the wall assemblies in comparison, while the walls with galvanized steel ties (UG models), the high conductivity material, have the least thermal resistance value, for which R_{eff} values are lower than the exterior insulation's R-value. Results of the stainless steel ties' models (US models) show a similar R_{eff} value as the exterior insulation's R-value used in the wall assembly. In Figure 4.9, the slope of the results for all types of tie decrease. The finding indicates that the reduction impact of ties on the R_{eff} value increases in higher insulation level walls. For wall assemblies with high thermal conductivity ties, the effectiveness of increasing the thermal insulation is diminished. For GFRP ties, due to the low thermal conductivity, the R_{eff} of the wall is almost the same as the performance without thermal bridging. Therefore, the thermal conductivity of the tie is an essential factor affecting the R_{eff} value of the wall assembly and the tie's thermal bridging can be eliminated by changing the tie material to a low thermal conductivity material. The percentage changes in each comparison group (e.g., using lower thermal conductivity tie material when the insulation R-value is constant and using higher insulation R-values when the tie material is fixed) are presented in Table 4.10 and Table 4.11.

Table 4.9: R_{eff} value of cases with different tie material ($m^2 \cdot K/W$)

Insulation Label	R15	R20	R25
UN: wall without tie	3.30	4.18	5.07
UG: Galvanized steel tie	2.52	3.08	3.56
US: Stainless steel tie	2.89	3.64	4.34

UF: GFRP tie	3.30	4.18	5.05
Insulation only	2.65	3.53	4.41

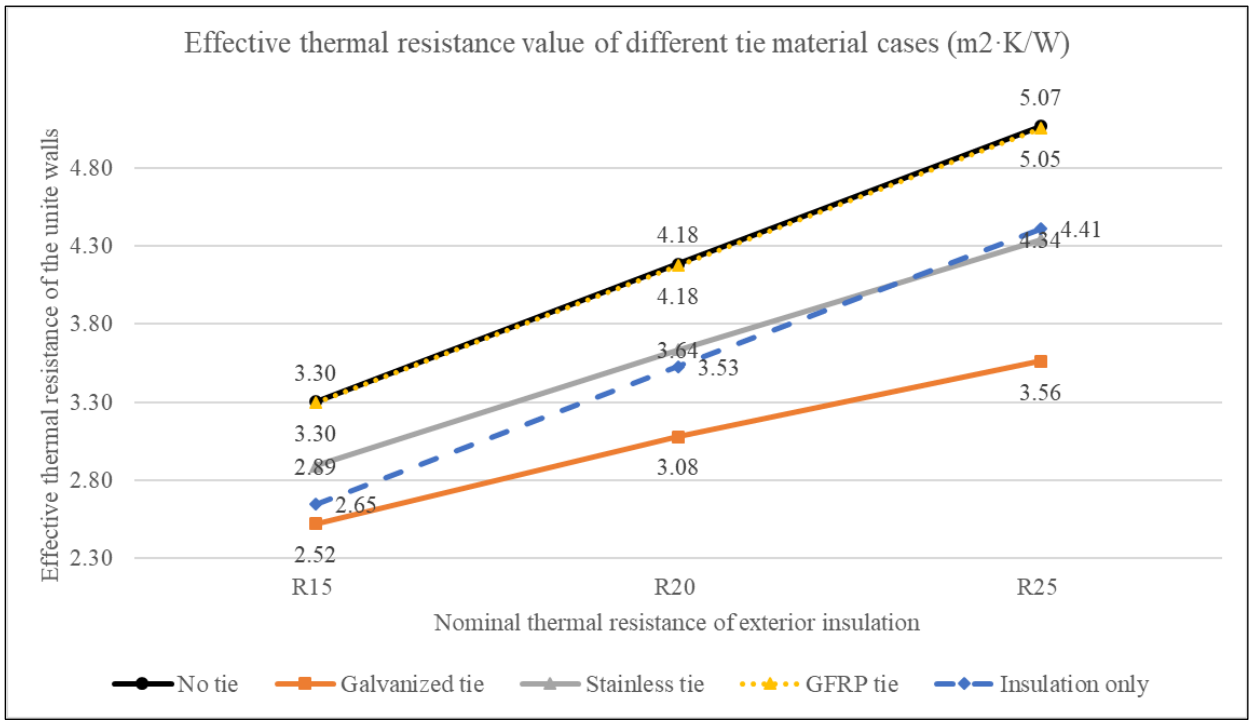

Figure 4.9: R_{eff} value of cases with different tie material (m^2·K/W).

Table 4.10: R_{eff} values of cases with different tie material and the percentage change with change in tie material (UG walls as the reference values) (m^2·K/W)

Insulation label	R15		R20		R25	
	R_{eff} (m^2·K/W)	Percentage change	R_{eff} (m^2·K/W)	Percentage change	R_{eff} (m^2·K/W)	Percentage change
UG: Galvanized steel tie	2.52	-	3.08	-	3.56	-
US:	2.89	14.68%	3.64	18.18%	4.34	21.91%

Stainless steel tie UF: GFRP tie	3.3	30.95%	4.18	35.71%	5.05	41.85%

Table 4.11: R_{eff} values of cases with different tie material and the percentage change with higher insulation R-value (R15 walls as the reference values) (m^2·K/W)

Wall Type	UG: Galvanized steel tie		US: Stainless steel tie		UF: GFRP tie	
	R_{eff} (m^2·K/W)	Percentage change	R_{eff} (m^2·K/W)	Percentage change	R_{eff} (m^2·K/W)	Percentage change
R15	2.52	-	2.89	-	3.3	-
R20	3.08	22.22%	3.64	25.95%	4.18	26.67%
R25	3.56	15.58%	4.34	19.23%	5.05	20.81%

4.2.3 Depth of the Tie inside the CMU

The impact of the tie depth in the CMU backup wall is presented in this section. Figure 4.10 presents the temperature distribution of model UG15. The temperature distribution of model UG15_D170 and UG15_D150 are similar to that of UG15. The heat flux was investigated on the inner CMU surface.

The penetration depth of the tie in the interior wythe of the wall has a small effect on the thermal performance of the wall, as shown from the results of ties with the same cross-sectional area and same contact area with the mortar. Similar temperature distributions were shown for the three models. Figure 4.11 shows the heat flux distribution on the interior surface (interior side of the concrete blocks backup wall) for the models in each case. The maximum and average heat flux values, as well as the R_{eff} value for each wall, are presented in Table 4.12. A higher maximum heat flux value was observed when the end of the tie is closer to the inner CMU backup wall surface, while the minimum and average heat flux values of the three cases are similar. Results show that the R_{eff} values of the assemblies have a small drop when the length of the tie decreases.

Therefore, shortening the tie depth in the backup wall can decrease the maximum heat flux value through the wall assembly but cannot make a considerable impact on the R_{eff} value of the assembly.

Consequently, results show that the tie depth is an insignificant parameter for addressing the tie's thermal bridging effect. The R_{eff} improvements resulting from decreasing the tie depth did not exceed 1%, which is considered to be insignificant.

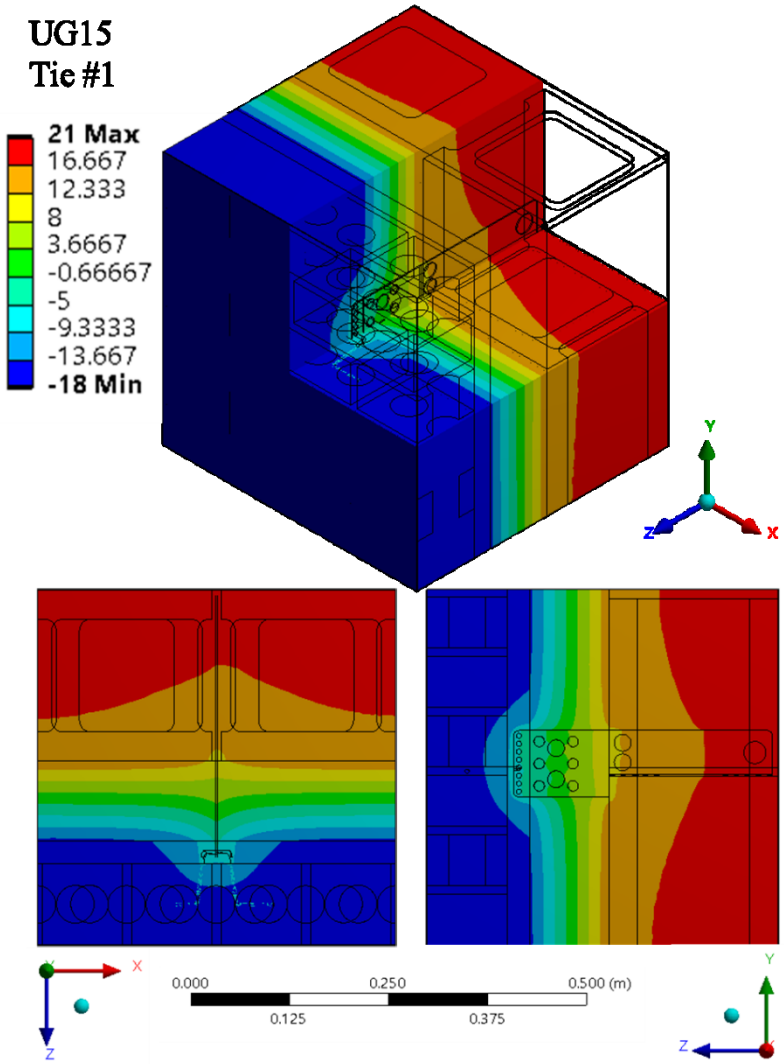

Figure 4.10: Temperature distribution for different UG15 walls with different view angle (℃).

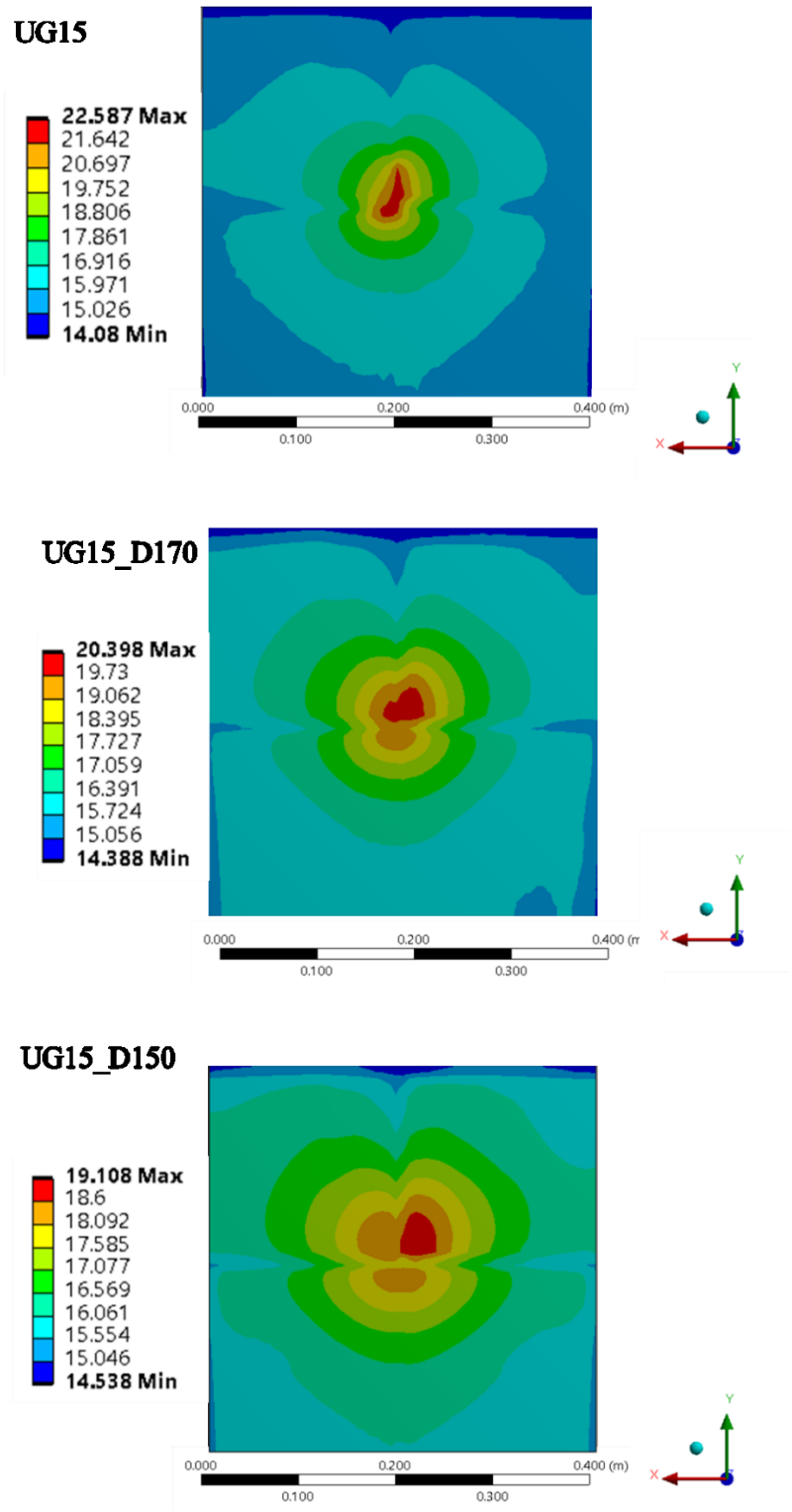

Figure 4.11: Heat flux distribution on the interior surface for walls with different tie depth (W/m^2).

Table 4.12: Data for different tie depth walls

	Maximum heat flux value (W/m^2)	Minimum heat flux value (W/m^2)	Average heat flux value (W/m^2)	R_{eff} value of the model ($m^2 \cdot K/W$)	R_{eff} Percentage change (%)
UG15	21.29	13.41	15.46	2.52	
UG15_D170	19.42	13.79	15.70	2.48	-1.48%
UG15_D150	17.94	13.55	15.55	2.51	-0.55%

4.2.4 Tie Spacing

Four walls assemblies with different tie spacing were addressed; UG15 (400 × 400 mm), UG15_S64 (600 × 400 mm), UG15_S84 (800 × 400 mm), and UN15 with no ties. To study the effect of different tie spacing on the effective thermal resistance, the assemblies' R_{eff} values were compared to the no-tie case. Table 4.13 shows the results of UG15, UG15_S64, UG15_S84, and the no-tie case UN15. Results show that increasing the tie spacing from 400 x 400 to 400 x 600 causes an improvement in the R_{eff} value of 7.13%, with an R_{eff} value increase up to 12.46% in the case of doubling the tie's spacing. By doubling the tie spacing, an 18% reduction in R_{eff} was observed compared to the no-tie case (UN15).

Figure 4.12 presents the heat flux distribution on the interior surface of the concrete backup wall for each model. Figure 4.13 shows the temperature distributions for all assemblies. The temperature distribution shows that the tie's thermal bridging effect is reduced by increasing the tie spacing. Figure 4.14 shows the relation between the R_{eff} values of the specimens and the tie spacing with the results of the no-tie case for comparison.

Table 4.13: Data for different tie spacing walls

	Maximum heat flux value (W/m^2)	Minimum heat flux value (W/m^2)	Average heat flux value (W/m^2)	R_{eff} value ($m^2 \cdot K/W$)	Percentage change (%)
UG15	21.29	13.41	15.46	2.52	
UG15_S64	20.59	12.72	14.44	2.70	7.13%
UG15_S84	20.27	11.26	13.75	2.84	12.46%
UN15	12.09	10.60	11.81	3.30	30.96%

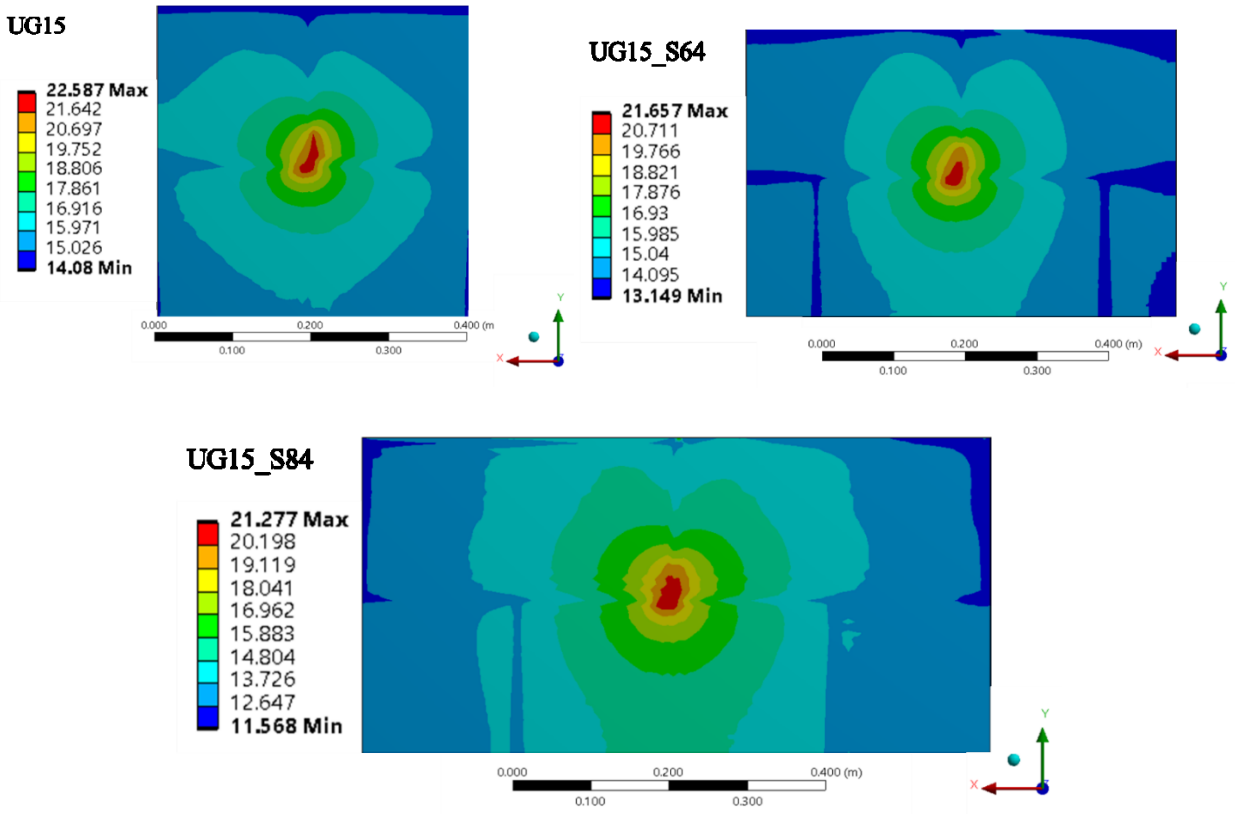

Figure 4.12: Heat flux distribution on the interior surface for different tie spacing walls (W/m^2).

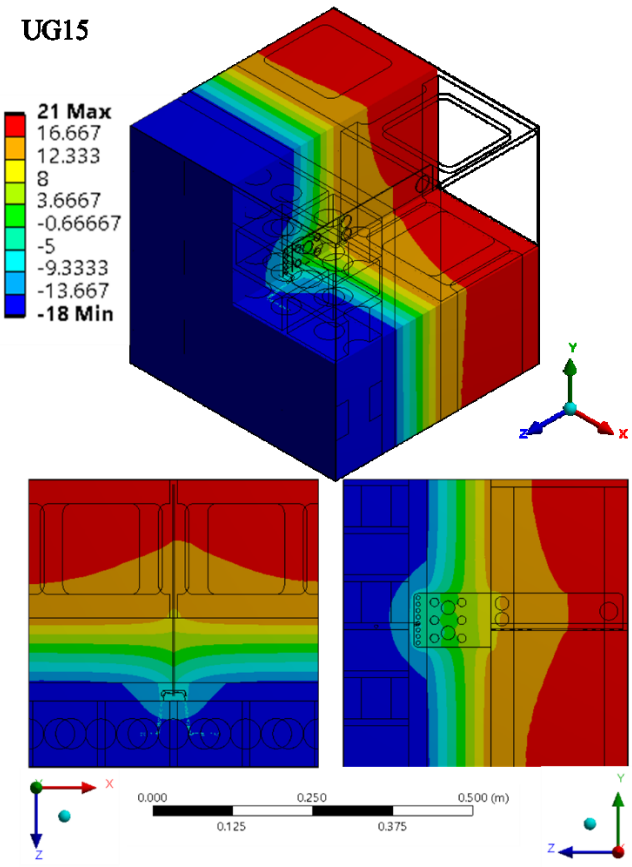
UG15
21 Max
16.667
12.333
8
3.6667
-0.66667
-5
-9.3333
-13.667
-18 Min
0.000
0.250
0.500 (m)
0.125
0.375

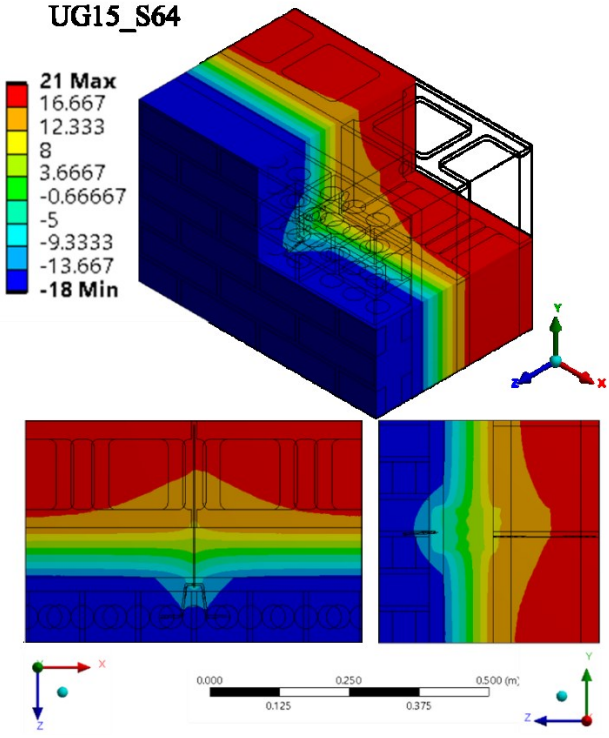
UG15_S64
21 Max
16.667
12.333
8
3.6667
-0.66667
-5
-9.3333
-13.667
-18 Min
0.000
0.250
0.500 (m)
0.125
0.375

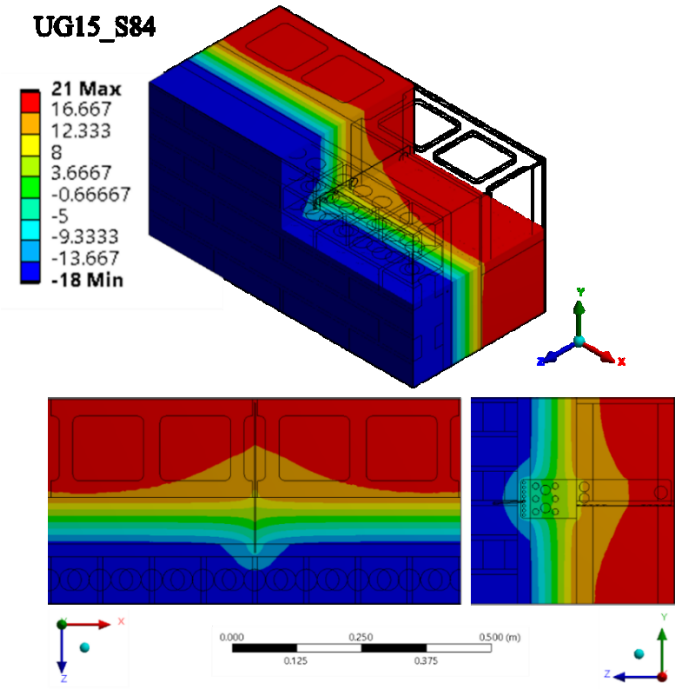

Figure 4.13: Temperature distribution for different tie-spacing models with different view angles (℃).

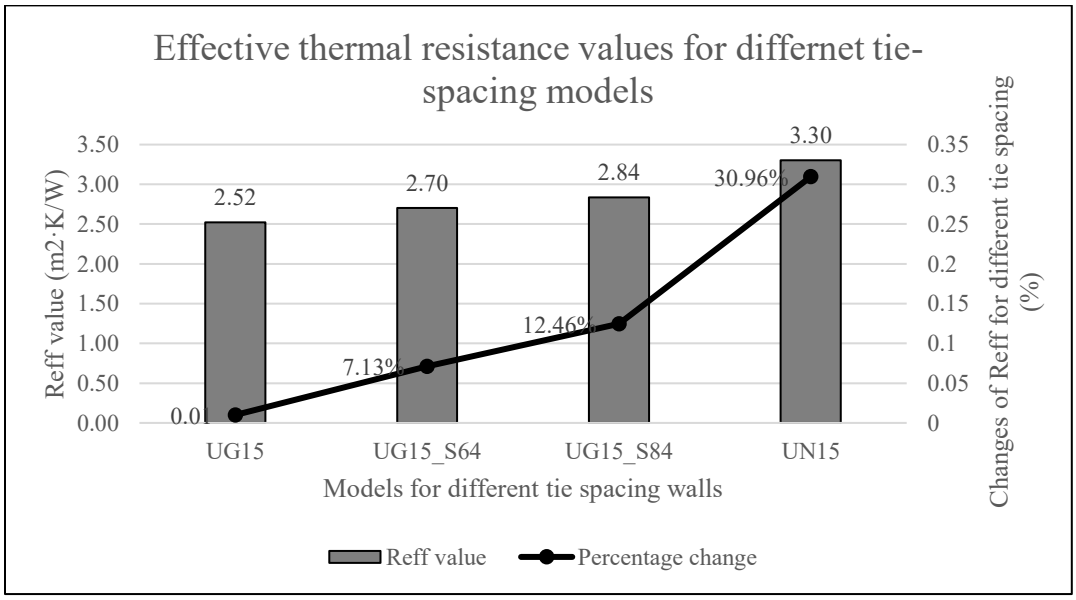

Figure 4.14: The R_{eff} values of the different tie-spacing models, and the percent changes.

4.2.5 Adding a Tie Insulation to Improve the Thermal Performance of the Wall

Figure 4.15 shows the temperature distribution of four models: with insulated ties, the original model UG15, and the no-tie model UN15. The heat flux and R_{eff} values of the addressed models are presented in Table 4.14. Results showed that when a tie is fully covered by thermal insulation, the R_{eff} value of the model increases from 1% to 2.1%. Therefore, it was concluded that adding up to 10 mm of insulation (thermal breaker) around the tie can have a minor improvement on the R_{eff} value. Figure 4.16 shows the heat flux distribution on the interior surface for concrete backup inner surface with different tie insulations.

Table 4.14: Data of the models having an insulation cover around tie body

	Maximum heat flux value (W/m^2)	Minimum heat flux value (W/m^2)	Average heat flux value (W/m^2)	R_{eff} value ($m^2 \cdot K/W$)	Percentage change (%)
UG15	21.29	13.41	15.46	2.52	
UIG15_F	21.83	10.68	15.31	2.55	1.03%
UIG15_F_10	21.13	11.77	15.14	2.58	2.13%

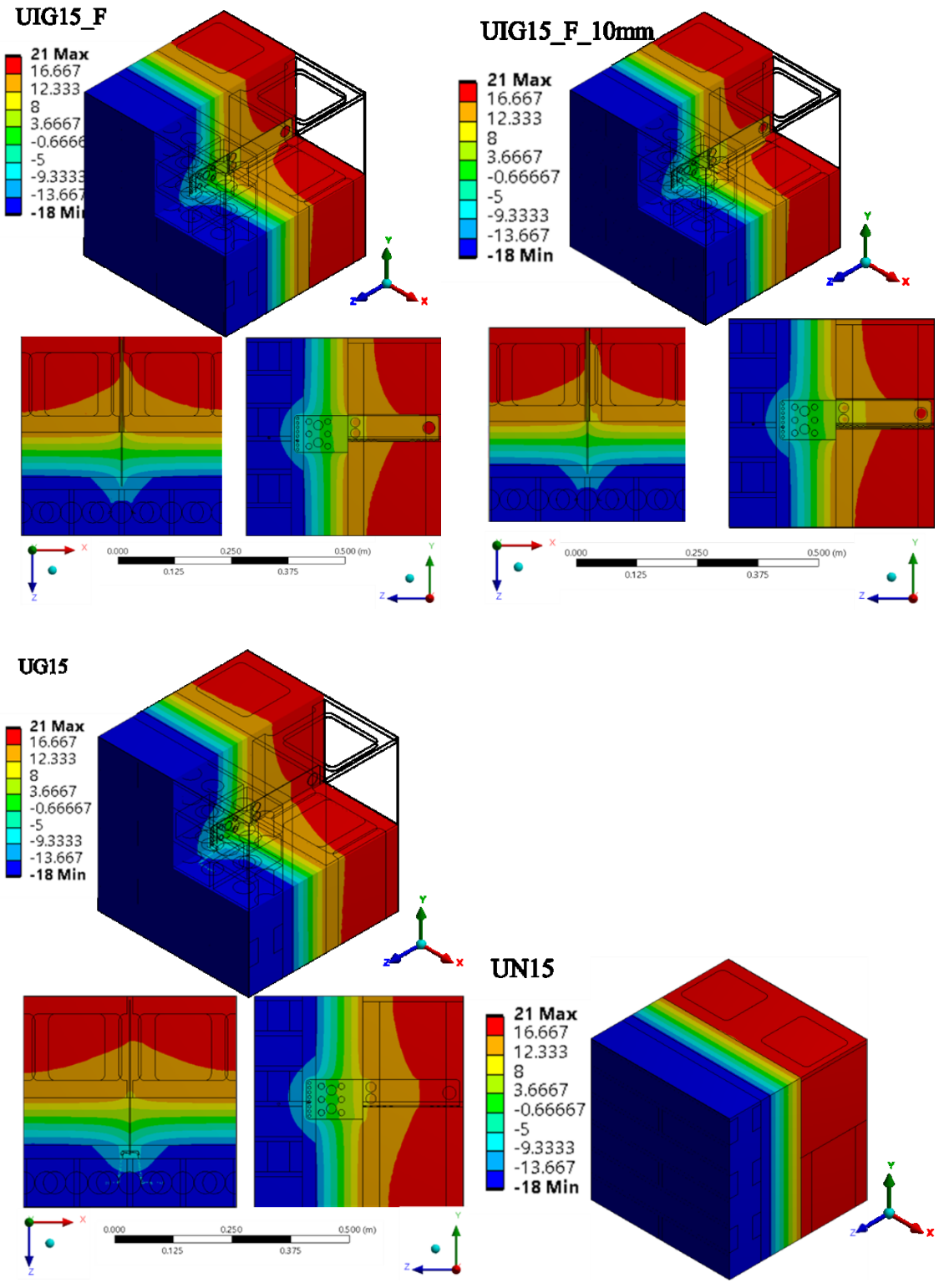

Figure 4.15: Temperature distribution for different UIG15 models with different view angle (℃).

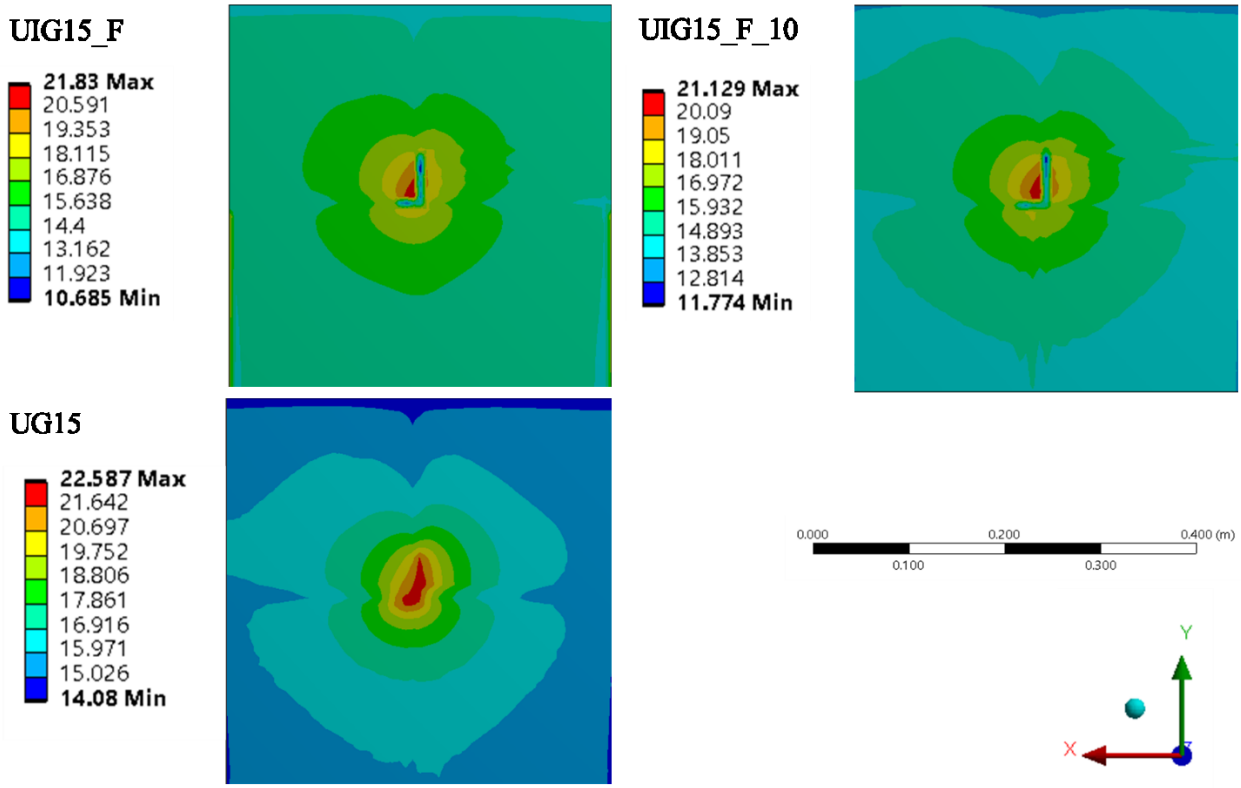

Figure 4.16: Heat flux distribution on the interior surface for walls with different thermal breaks (W/m^2).

4.3 Section Conclusion

This chapter presents the R-value results obtained from the air gap analysis, in addition to a parametric analysis investigating the influencing factors affecting the tie's thermal resistance (e.g., material, depth, spacing and adding thermal breaks around the ties).

An R-value of 0.135 $m^2 \cdot K/W$ was obtained in the case of a wall assembly with uniformly spaced ties and a 25-mm air gap. It was concluded that the rigid insulation board level (R-value) and air velocity in the air gap are significant influence factors on the effective thermal resistance of the air gap. In practice, the R15 and higher rigid insulation boards are commonly used. Therefore, the effective thermal resistance of the air gap obtained from the model WG15 (0.135 $m^2 \cdot K/W$) is sufficiently representative of the majority of the air gap's thermal resistance used in construction. By comparing the effective thermal resistance of the air gap obtained from this study and the values from the literature, it was concluded that the ventilation of the air gap and the metal tie's thermal

bridges significantly affect the thermal resistance of the air gap in the wall assembly, with an effect ranging from 15.6% to 47.2%.

The CMU voids R-value results vary based on the chosen simulation method. However, due to the limitations in identifying an accurate mean temperature in the cores and temperature difference in the block, an accurate determination of convective coefficient is not possible. Therefore, an equivalent method was used to set up the properties of the air in the CMU block.

The parametric analysis addressed the impact of each studied parameter on the overall thermal properties of the wall. Using a low thermal conductive tie, such as a GFRP tie, can effectively eliminate the impact of the tie's thermal bridging. Enlarging the tie spacing can also improve the thermal resistance of the whole wall by up to 12%. Adding a thin insulation cover to the tie body can only increase the R_{eff} value by a maximum of 2.1%. However, other parameters, such as the depth of the tie and the grout conditions in the CMU backup wall, are not effective in the thermal improvement to the wall assembly.

5 Conclusions

Masonry ties can cause a considerable reduction in thermal resistance in building envelopes. Moreover, the tie's thermal bridging effect can increase the energy consumption of buildings. Several literature surveys have shown that veneer ties significantly reduce the thermal resistance of masonry walls. Although previous studies have already addressed the impact of a tie on reducing the thermal resistance of walls, the thermal impact of the tie was not comprehensively studied and little attention has been considered for the reduction effect on the R-value of a tie in the thermal design of a building. For example, the air gap between the brick veneer and insulation board in masonry cavity walls must be further addressed and the impact of ties on the thermal resistance of the wall assembly has not been addressed for all possible influence factors. Therefore, this thesis presents a study to determine the effective thermal resistance of the ventilated air gap in the masonry cavity wall using finite element models. In addition, a parametric analysis was performed to study the variations in tie material, nominal R-value insulation, tie depth and spacing, grout condition in the CMU voids, and effect of adding insulation around the tie. Based on the analyzed results, improvement strategies are suggested to reduce the tie's thermal bridging effect and enhance the thermal resistance of the wall.

5.1 Conclusion Remarks

The conclusion of this study is summarized as follows:

- The effective thermal resistance of a 25-mm air gap ranges from 0.12 m^2·K/W to 0.15 m^2·K/W in the case of a ventilated air gap with the presence of veneer ties interrupting the airflow through the air gap between the brick veneer and insulation board. In the case of R15 insulation boards, the effective thermal resistance of the air gap was found to be 0.135 m^2·K/W.
- The insulation R-value and airflow velocity through the air gap have a significant impact on the effective thermal resistance of the air gap. Using a higher insulation R-value showed remarkable improvement in the effective thermal resistance of the air gap. When the insulation R-value increased to R5, the improvement of the R_{eff} value of the wall can reach up to 26%. In addition, the air gap's effective thermal resistance was improved by approximately 15% to 20% in the case of reducing the airflow velocities from 0.15 m/s to 0.05 m/s. However, the R_{eff} value of the wall assembly is only affected by 1%, suggesting

that changing the air velocity in the air gap has an insignificant impact on the overall thermal resistance of the wall.

- By comparing the obtained effective thermal resistance of the air gap using CFD simulations and the thermal resistance value of the vertical air layer selected from codes and reports, such as ISO 6946, ASHRAE Fundamental Handbook, and Morrison Hershfield's catalog, the air gap ventilation and tie's thermal bridging effect was found to reduce the effective thermal resistance of the air gap by up to 47.2%.
- The tie material has the most significant impact on the effective thermal resistance of masonry walls. Using GFRP ties can almost eliminate the ties thermal bridging effect; as a result, the thermal resistance of the GFRP-tie walls is the same as the no-tie walls. Using the stainless steel ties can cause an improvement of 14.7% to 21.9% compared to using galvanized steel ties in the wall assembly. Tie spacing has a significant impact on the effective thermal resistance of masonry walls. By doubling the tie spacing in one direction, the thermal resistance of the wall can be improved by up to 12%.
- Using a low thermal conductivity tie material such as GFRP is recommended for effective R-value improvement. In addition, increasing the tie spacing can significantly alleviate the tie's thermal bridge reduction effect.
- The tie depth in the CMU backup wall and grout conditions of the CMU voids had an insignificant impact on the wall's effective thermal resistance.
- Adding a thin insulation layer around the end of the tie body did not result in a significant reduction of the tie's thermal bridging effect. This approach increased the effective thermal resistance of the wall assembly by a maximum of 2.1%.

5.2 Future Recommendations

Further research is needed to address the effect of natural convection and radiation on CMU cores. The feasibility of using an equivalent CMU layer in the thermal resistance evaluation of masonry cavity walls instead of fluid analysis (CFD) in the thermal analysis must be further investigated. In addition, experimental investigations are required for verification purposes and improvements to the finite element simulations.

References

Ancon, 2021. Introducing the New Bond.

Andrea Love, C.K., 2011. Thermal Bridging: Observed Impacts and Proposed Im-provement for Common Conditions.

ANSYS, 2021. Ansys Fluent Theory Guide. ANSYS Inc., USA 15317, 724–746.

Arendt, K., Krzaczek, M., Florczuk, J., 2011. Numerical analysis by FEM and analytical study of the dynamic thermal behavior of hollow bricks with different cavity concentration. Int. J. Therm. Sci. 50, 1543–1553. https://doi.org/10.1016/j.ijthermalsci.2011.02.027

Ashrae, 2017. Chapter 27 Heat , Air , and Moisture Control in Building Assemblies — Examples, in: ASHRAE Handbook-Fundamentals. pp. 25.1-25.16.

ASHRAE, 2017a. Chapter 25, Heat,air and moisture control in building assemblies fundamentals, in: AHSRAE Handbook-Fundamentals. p. 22.

ASHRAE, 2017b. Chapter 26 Heat, air, and moisture control in building assemblies - Material properties, in: ASHRAE Handbook - Fundamentals. p. 22.

ASTM C1058, 2015. Standard Practice for Selecting Temperatures for Evaluating and Reporting Thermal Properties of Thermal Insulation. ASTM Int. 10, 1–4. https://doi.org/10.1520/C1058-10.2

Bontha, S., Klingbeil, N.W., Kobryn, P.A., Fraser, H.L., 2006. Thermal process maps for predicting solidification microstructure in laser fabrication of thin-wall structures. J. Mater. Process. Technol. 178, 135–142. https://doi.org/10.1016/j.jmatprotec.2006.03.155

CAN/CSA-A370-14, 2015. National Standard of Canada:CAN/CSA-A370-14 Connnectors for masonry.

Capozzoli, A., Gorrino, A., Corrado, V., 2013. A building thermal bridges sensitivity analysis. Appl. Energy 107, 229–243. https://doi.org/10.1016/j.apenergy.2013.02.045

Cavanaugh, K., Speck, J.F., 2002. Guide to Thermal Properties of Concrete and Masonry Systems Reported by ACI Committee 122. Concrete 1–21.

CLEAR, 2004. Cavities and air spaces [WWW Document]. Comf. low energy Archit. URL https://www.new-learn.info/packages/clear/thermal/buildings/building_fabric/elements/cavities_and_air_spaces.html

Drysdale, R.G., Hmid, A.A., 2005. Masonry Structures Behaviour and Design, 4th ed. Canadian masonry design center.

Fero, n.d. Block shear ™. Edmonton.

Fioretti, R., Principi, P., 2014. Thermal performance of hollow clay brick with low emissivity treatment in surface enclosures. Coatings 4, 715–731.

https://doi.org/10.3390/coatings4040715

Gao, Y., Roux, J.J., Zhao, L.H., Jiang, Y., 2008. Dynamical building simulation: A low order model for thermal bridges losses. Energy Build. 40, 2236–2243. https://doi.org/10.1016/j.enbuild.2008.07.003

Gregory, K., Moghtaderi, B., Sugo, H., Page, A., 2008. Effect of thermal mass on the thermal performance of various Australian residential constructions systems. Energy Build. 40, 459–465. https://doi.org/10.1016/j.enbuild.2007.04.001

Hassid, S., 1990. Thermal bridges across multilayer walls: An integral approach. Build. Environ. 25, 143–150. https://doi.org/10.1016/0360-1323(90)90026-N

Hatzinikolas, M.A., Korany, Y., Brzev, S., 2015. Masonry Design For Engineers and Architects (Fourth Edition), Fourth Edi. ed.

Hendry, E.A.W., 2001. Masonry walls: Materials and construction. Constr. Build. Mater. https://doi.org/10.1016/S0950-0618(01)00019-8

Henrique Dos Santos, G., Fogiatto, M.A., Mendes, N., 2017. Numerical analysis of thermal transmittance of hollow concrete blocks. J. Build. Phys. 41, 7–24. https://doi.org/10.1177/1744259117698522

Ibañez-Puy, M., Vidaurre-Arbizu, M., Sacristán-Fernández, J.A., Martín-Gómez, C., 2017. Opaque Ventilated Façades: Thermal and energy performance review. Renew. Sustain. Energy Rev. 79, 180–191. https://doi.org/10.1016/j.rser.2017.05.059

Inoue, T., Hayakawa, K., Suzuki, Y., 2013. Thermal conductivity measurement of GFRP at cryogenic temperature. ICCM Int. Conf. Compos. Mater. 2013-July, 2261–2268.

ISO 6946, 2017. INTERNATIONAL STANDARD ISO 6946 Building components and building elements — Thermal resistance and thermal transmittance — Calculation methods.

ISO6946:2007(E), 2007. International Standard Iso 6946:2007(E) 2007.

Laaroussi, N., Lauriat, G., Raefat, S., Garoum, M., Ahachad, M., 2017. An example of comparison between ISO Norm calculations and full CFD simulations of thermal performances of hollow bricks. J. Build. Eng. 11, 69–81. https://doi.org/10.1016/j.jobe.2017.03.011

Leviat, 2021. Wall ties and restraint fixings for the construction industry.

Lissel, S.L., Shrive, N.G., 2001. Glass fibre reinforced polymer (GFRP) shear connectors for masonry, in: Proceedings, 9th Canadian Masonry Symposium, Fredericton, New Brunswick. On CD.

Martínez, M., Huygen, N., Sanders, J., Atamturktur, S., 2018. Thermo-fluid dynamic analysis of concrete masonry units via experimental testing and numerical modeling. J. Build. Eng. https://doi.org/10.1016/j.jobe.2018.04.029

Mingotti, N., Chenvidyakarn, T., Woods, A.W., 2011. The fluid mechanics of the natural

ventilation of a narrow-cavity double-skin facade. Build. Environ. 46, 807–823. https://doi.org/10.1016/j.buildenv.2010.09.015

Molina-Aiz, F.D., Fatnassi, H., Boulard, T., Roy, J.C., Valera, D.L., 2010. Comparison of finite element and finite volume methods for simulation of natural ventilation in greenhouses. Comput. Electron. Agric. 72, 69–86. https://doi.org/10.1016/j.compag.2010.03.002

Mooneghi, M.A., Kargarmoakhar, R., Chowdhury, A.., 2015. Improving the Thermal Performance of Concrete Masonry Blocks. Florida Civ. Eng. J. 1–10.

Morrison Hershfield, 2018a. Building Envelope Thermal Bridging Guide 35.

Morrison Hershfield, 2018b. Appendix a – Catalogue Material Data Sheets. Build. Envel. Therm. Bridg. Guid.

National Concrete Masonry Association, 2012. Thermal Catalog of Concrete Masonry Assemblies. NCMA Publ. 2nd, 1–96.

NECB, 2017. National Energy Code of Canada for Buildings 2017.

NRCan (Natural Resources Canada), 2014. Canada's Secondary Energy Use by Sector, End Use and Subsector. Energy Use Data Handb. Tables.

NSAI, 2017. ISO 6946 The National Standards Authority of Ireland (NSAI) produces the following categories of formal documents.

Roppel, P., Lawton, M., Norris, N., 2012. Thermal performance of building envelope details for mid- and high-rise buildings. ASHRAE Trans. 118, 569–584.

Sanjuan, C., Suárez, M.J., González, M., Pistono, J., Blanco, E., 2011. Energy performance of an open-joint ventilated façade compared with a conventional sealed cavity façade. Sol. Energy 85, 1851–1863. https://doi.org/10.1016/j.solener.2011.04.028

Stovall, T.K., Karagiozis, A., 2004. Airflow in the Ventilation Space behind a rain screen wall 11.

Straka, V., 2013. Composite masonry wall ties: final report.

Sun, J., Fang, L., 2009. Numerical simulation of concrete hollow bricks by the finite volume method. Int. J. Heat Mass Transf. 52, 5598–5607. https://doi.org/10.1016/j.ijheatmasstransfer.2009.06.008

Tejedor, B., Barreira, E., Almeida, R.M.S.F., Casals, M., 2020. Thermographic 2D U-value map for quantifying thermal bridges in building façades. Energy Build. 224, 110176. https://doi.org/10.1016/j.enbuild.2020.110176

Theodosiou, T.G., Tsikaloudaki, A.G., Kontoleon, K.J., Bikas, D.K., 2015. Thermal bridging analysis on cladding systems for building facades. Energy Build. 109, 377–384. https://doi.org/10.1016/j.enbuild.2015.10.037

Ujma, A., Umnyakova, N., 2019. Thermal efficiency of the building envelope with the air layer

and reflective coatings. E3S Web Conf. 100. https://doi.org/10.1051/e3sconf/201910000082

Wilson, M., Higgins, J., 2014. FERO RAP TIE AND FAST SYSTEM THERMAL ANALYSIS Background & Energy Code Requirements for Walls in Canada. Vancouver.